國立臺灣大學理學院物理學研究所

碩士論文

Graduate Institute of Physics

College of Science

National Taiwan University

Master Thesis

分子束磊晶成長鋁奈米薄膜中之拓撲相變與違反包立順磁極限之現象

Topological transition and violation of Pauli paramagnetic limit in Al nanofilms grown by molecular beam epitaxy

葉勁辰

Ching-Chen Yeh

指導教授：梁啟德 博士

Advisor: Dr. Chi-Te Liang FInstP

中華民國 108 年 7 月

July, 2019

致謝

這篇論文之所以能夠順利完成，要感謝許多人的幫忙與協助。

首先要非常感謝梁啟德老師的指導，讓我在碩班期間能夠有一個明確的方向，並在實驗上提供許多協助，同時也和我們分享一些相關文獻，最後在論文撰寫上也給予了相當的修訂意見，才使這篇論文能夠順利完成。

感謝交大的林聖迪老師教授與范雁婷學姊製作了高品質的鋁奈米薄膜以提供量測，並且提供詳細的製程相關資料與樣品數據。

感謝稟弋學長在量測程式上的協助，使得量測非常順利。在實驗上也提供了許多有用的經驗，並且教導了很多實驗技巧與該注意的事項。

感謝冠銘學長與朝興學長無論在修課上或實驗上都願意分享與提供有用的建議，並且在分析數據上也提供了相當的幫助。

感謝偉仁、昱辰、致元在實驗上的幫忙與協助，也常常在討論中給予相當有用的建議。

最後也感謝家人的支持，讓我能夠一直朝著目標前進。

摘要

在這篇論文中，我將會報告利用分子束外延(molecular beam epitaxy)成長在砷化鎵(GaAs)上的鋁奈米薄膜(Al nanofilms)在低溫下表現的傳輸特性。利用此方法所成長的鋁奈米薄膜比傳統的鋁塊材擁有較高的臨界溫度與臨界磁場。特別的是，在這樣的鋁奈米薄膜中觀察到拓撲相變(topological transition)，這表示我們的鋁奈米薄膜可是被視為二維系統。另外也發現在最薄的樣品中(3-nm)平行的上臨界磁場(upper critical magnetic field)能夠超過包立順磁極限(Pauli paramagnetic limit)。

關鍵字：超導電性、鋁奈米薄膜、包立順磁極限、拓撲相變

ABSTRACT
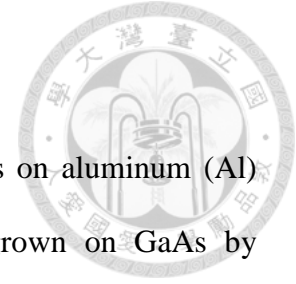
In this thesis, I shall report extensive transport measurements on aluminum (Al) nanofilms (as-grown thickness ranging from 3 nm to 4 nm) grown on GaAs by molecular beam epitaxy (MBE). Such MBE-grown Al nanofilms have a higher superconductor transition temperature (around 2.17 K, depending on the thickness) compared to that of bulk aluminum (1.2 K). In particular, I observed the topological transition of Berezinskii-Kosterlitz-Thouless (BKT) transition which implies two-dimensional superconductivity in our system. I also found that the upper critical field goes beyond the Pauli paramagnetic limit in the thinnest sample (3-nm thick).

Keywords: superconductivity, aluminum nanofilms, Pauli paramagnetic limit, topological transition

CONTENTS

iv

LIST OF FIGURES

LIST OF TABLES

Chapter 1   Introduction

In 2010, the Nobel Prize in physics was awarded to Andre Geim and Konstantin Novoselov for their work on graphene, which is a two-dimensional (2D) material [1]. The 2D system has attracted much attention. With progress in science and technology, we can grow high quality thin film like aluminum, graphene, MoS_2, and so forth with a scalable size, controllable thickness [2, 3]. As a result, we are allowed to further investigate the 2D systems.

In this work, I have performed extensive transport measurement on aluminum (Al) nanofilms on GaAs grown by molecular beam epitaxy (MBE) which exhibit superconducting behavior below the critical temperature. Interestingly, the critical temperature is higher than that conventional bulk aluminum (1.2 K) and the critical magnetic field exceeds the Pauli paramagnetic limit [4, 5].

Nowadays, superconductors are widely utilized such as superconducting magnets, Maglev and nuclear magnetic resonance. However, liquid helium is expensive and plays an important role in cooling a conventional superconducting system. Luckily we have a cryo-free dilution refrigerator, which only relies on electricity, for probing superconductivity in Al nanofilms grown by MBE.

REFERENCES

[1]   M. I. Katsnelson and K. S. Novoselov, *Solid State Communications,* 143, 3 (2007).

[2]   Y.-T. Fan, M.-C. Lo, C.-C. Wu, P.-Y. Chen, J.-S. Wu, C.-T. Liang, and S.-D. Lin, *AIP Adv*. 7, 075213 (2017).

[3]   Albert F. Rigosi, Chieh-I Liu, Bi-Yi Wu, Hsin-Yen Lee, Mattias Kruskopf, Yanfei Yang, Heather M. Hill, Jiuning Hu, Emily G. Bittle, Jan Obrzut, Angela R. Hight Walker, Randolph E. Elmquist, and David B. Newell, *Microelectronic Engineering* 194, 51 (2018).

[4]   A. M. Clogston, *Phys. Rev. Lett.* 9, 6 (1962).

[5]   B. S. Chandrasekhat, *Appl. Phys. Lett.* 1, 1 (1962).

Chapter 2 Superconductivity

Superconductivity was discovered by Heike Kamerlingh Onnes in 1911 [1]. When the temperature is lower than the critical temperature, where the phase transition takes place, some materials exhibit superconducting behavior. In the superconducting state, resistivity becomes zero and the material excludes the applied external magnetic field from the interior which is called the Meissner-Ochsenfeld effect [2] as shown in figure 2.1.
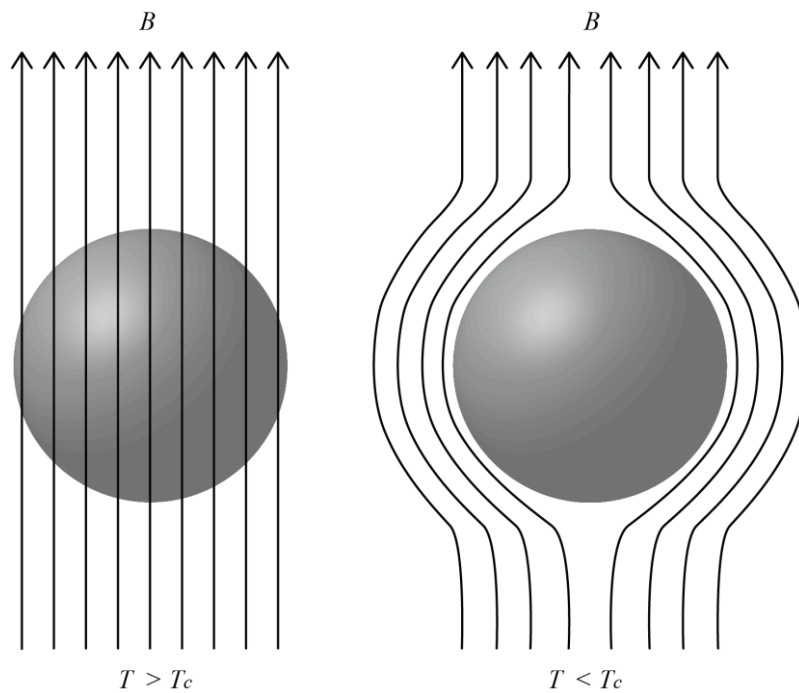
Figure 2.1 Meissner-Ochsenfeld effect. As $T > T_c$, the magnetic field can enter into the interior of a type-I superconductor. As $T < T_c$, the magnetic field is excluded from the interior.

3
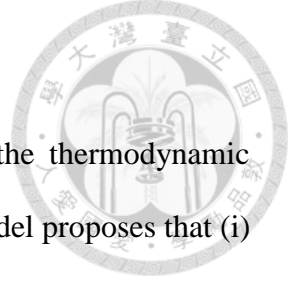
2.1 Two-fluid Model

Gorter and Casimir proposed a two-fluid model to explain the thermodynamic properties of superconducting phase transition [3]. The two-fluid model proposes that (i) there are two types of free electron, one is normal electron, the other one is superconducting electron which depends on temperature. (ii) a normal electron can scatter with lattice so contribute to entropy and result in resistance (iii) a superconducting electron is in a condensed state which means superconducting electrons condense in lower energy state. When the phase transition occurs, the free energy of superconducting stat is lower than the free energy of normal state $(F_n - F_s = \frac{\mu_0 H_c^2}{2})$, where V is volume of superconductor. (iv) superconducting phase transition belong to second order transition and superconducting state is order state.

2.2 London Equations

In 1935, the following two equations were derived by London and London [4].

$$\vec{B} = -\frac{m}{n_s e^2} \nabla \times \vec{j_s},$$ (2.2.1)

$$\frac{\partial}{\partial t} \vec{j_s} = \frac{n_s e^2}{m} \vec{E},$$ (2.2.2)

where $\vec{j_s}$ is the superconducting current density, e is the charge of an electron, n_s is the number density of superconducting electrons, m is electron mass, $\vec{B}$ and $\vec{E}$ are the magnetic and electric field within the superconductor respectively.

Eq. (2.2.1) and Eq. (2.2.2) are called the first and the second London (LD) equations, respectively. Combining Ampere's law $\nabla \times \vec{B} = \mu_0 \vec{J}$ with the LD equation,

4

we have

$$\nabla^2 \vec{B} = \frac{1}{\lambda^2} \vec{B}.$$ (2.2.3)

The solution of Eq. (2.2.3) is

$$B_z(x) = B_0 e^{-\frac{x}{\lambda}}.$$ (2.2.4)

This implies that the external magnetic fields are exponentially screened with a characteristic length λ which is called the penetration depth. The penetration depth is

$$\lambda = \sqrt{\frac{m}{\mu_0 n_s e}}.$$ (2.2.5)

Using Ampere's law $\nabla \times \vec{B} = \mu_0 \vec{J}$ again with Eq. (2.4), we have

$$\vec{j_y} = \frac{B_a}{\mu_0 \lambda} e^{\left(-\frac{x}{\lambda}\right)}.$$ (2.2.6)

This implies that current can just flow on the surface with depth λ.

Although the LD equations are consistent with most experimental results, they cannot explain the mechanism of superconducting behavior. After that, with advances in theory, there are some widely acceptable theories which will be further discussed.

2.3   BCS Theory

In 1957, conventional superconductors were modeled successfully by the pioneering theory developed by John Bardeen, Leon Cooper and Robert Schrieffer in what is called the BCS theory [5]. The BCS theory is different from LD equations, phenomenology equation, and is the first microscopic theory of superconductivity [6]. They suggested that in the superconducting state the electron pairs by lattice vibration (phonon) and form the Cooper pair in which two electrons are bound to each other.

5

Such a revolutionized concept has won Bardeen, Cooper and Schrieffer the Nobel prize in Physics in 1972.
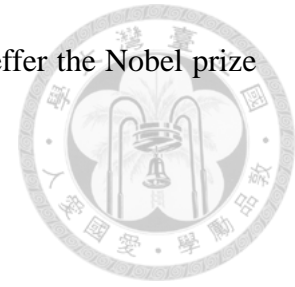
2.3.1 Cooper Pair

The Cooper pair was proposed by Cooper in 1956 [7]. The basic concept is that in addition to Coulomb repulsion there is some attraction between electrons to form a Cooper pair because the free energy reduces when normal state transfer to superconducting state. The mechanism can be simply explained by a classical method [8]. As shown in figure 2.1, an electron attracts the positive ions and increases the positive charge density nearby. Although there is Coulomb repulsion, this local positive charge area attracts another electron and then pair them up. It can also be explained by the quantum mechanical effect which shows that the attraction is due to electron-phonon interaction. The phonon is a collective vibrational motion of the positively charged lattice [9].
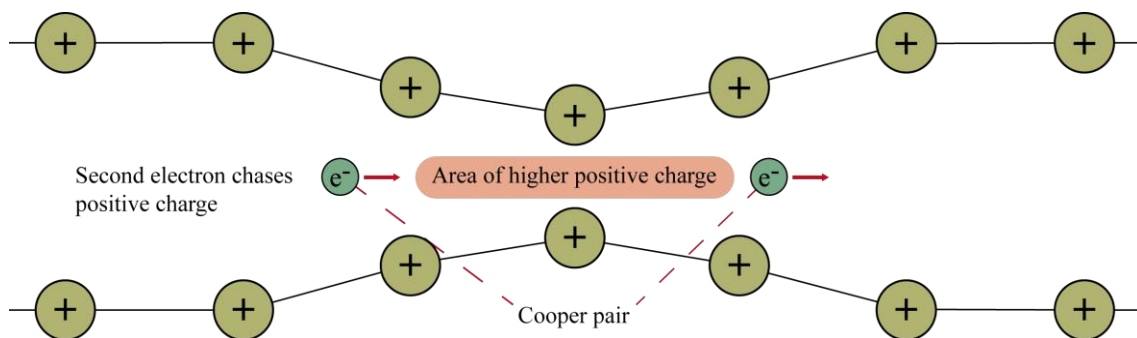
Figure 2.2 Cooper pair diagram.

Although electrons are fermion which cannot occupy the same quantum state due to the Pauli exclusion principle, Cooper pairs, which are composed of two electrons with opposite spin and momentum, are bosons and can occupy the same quantum state because the electron-phonon interaction is long range and the distance is usually greater than distance of electron [10].
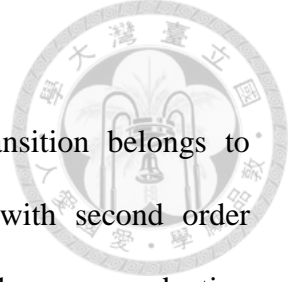
2.3.2 Energy Gap

As indicated in previous section superconducting phase transition belongs to second order transition. The physical quantity which correlate with second order transition is specific heat. From the experiment result in Ref.[11], the superconducting specific heat depends on temperature with exponential relation.

$$\frac{c_{es}}{\gamma T_c} = 9.17 e^{-1.5 T_c / T} .$$ (2.3.1)

In statistical mechanics, if there is an energy gap in a single electron system, with increasing temperature the electron must absorb the energy which is equal to energy gap in exciting process and the number of electron is proportional to $e^{\Delta / k_B T}$. Therefore, it is expected that there is an energy gap in superconducting state and the energy gap is 2Δ. The energy gap of BCS theory is given

$$\Delta = \frac{\hbar \omega_D}{\sinh\left(\frac{1}{N(0)V}\right)} \overset{N(0)V \ll 1}{\approx} 2\hbar \omega_D e^{-\frac{1}{N(0)V}} ,$$ (2.3.2)

where $N(0)$ is density of state on the Fermi surface, ω_D is Debye frequency.

2.4 Ginzburg-Landau Theory

After the development of the LD equations, Ginzburg also proposed a phenomenology theory which is called Ginzburg-Landau (GL) theory in 1950 and based on the theory of phase transition [12]. Although the GL theory was just a mathematical model for describing the superconducting behavior, Gor'kov prove that the GL theory is a limitation of BCS theory as $T \to T_c$ from the view of microscopic theory in 1957 [13].

7

In 1937, Landau proposed a theory of second order phase transition which based on the three postulates. First, there is an order parameter ψ which will be zero when a phase transition take place. Second, free energy can be expanded with ψ by power law. Third, the coefficient is the function of temperature.

Following Landau's postulates, Ginzburg developed the theory so-called Ginzburg-Landau (GL) theory and interpret the physics meaning of ψ as $|\psi|^2 = n_s$ where n_s is the density of superconducting electron. When $T \to T_c$, the free energy can be write as

$$F_s = F_n + \alpha_{GL}|\psi|^2 + \left(\frac{\beta_{GL}}{2}\right)|\psi|^4 + \frac{1}{2m^*}\left|\left(\frac{h}{i}\nabla - \frac{e^*}{c}\vec{A}\right)\psi\right|^2 + \frac{h^2}{8\pi}, \tag{2.4.1}$$

where F_s is the free energy of a superconductor, F_n is the free energy of a normal state, e^* is the charge of pair of electron and $e^* = 2e$, which e is the charge of single electron, $m^* = 2m$ and n_s^* is the number of pair of electron and $n_s^* = \frac{1}{2}n_s$, where n_s is the number of single electron in the condensate. The first two terms are from Landau's postulate. The third term is kinetic energy of superconducting electron. The last term is the energy which is induced by magnetic field.

2.4.1   Magnetic Field Dependence of Temperature

To figure out the parameters α_{GL} and β_{GL}, the case without field and gradient was discussed. Equation (2.4.1) becomes

$$F_s - F_n = \alpha_{GL}|\psi|^2 + \left(\frac{\beta_{GL}}{2}\right)|\psi|^4. \tag{2.4.2}$$

Evidently β_{GL} must be a positive value for the lowest free energy at the transition

point $T = T_c$ because the density of superconducting electron $n_s = |\psi|^2 \rightarrow 0$ as

$T \rightarrow T_c$. If the β_{GL} is a negative value, the minimum of free energy would occur with

any allowed value of $|\psi|^2$. Different from the value of β_{GL}, α_{GL} can be positive or

negative value. As $T < T_c$, α_{GL} is a negative value and the minimum of free energy

occurs at $|\psi|^2 = -\dfrac{\alpha_{GL}}{\beta_{GL}}$. As $T > T_c$, α_{GL} is a positive value and the minimum of free

energy occurs at $|\psi|^2 = 0$. Therefore $\alpha_{GL}(T)$ can be written as

$$\alpha_{GL}(T) = (T - T_c)\left(\dfrac{d\alpha_{GL}}{dT}\right)_{T=T_c}. \tag{2.4.3}$$

Now, substituting $|\psi|^2 = |\psi_\infty|^2 = -\dfrac{\alpha_{GL}}{\beta_{GL}}$ and $\alpha_{GL}(T) = (T - T_c)\left(\dfrac{d\alpha_{GL}}{dT}\right)_{T=T_c}$ into equation

(2.4.2)

$$F_s - F_n = -\dfrac{\alpha_{GL}{}^2}{2\beta_{GLc}} = -\dfrac{(T - T_c)^2}{2\beta_{GLc}}\left(\dfrac{d^2\alpha_{GL}}{dT^2}\right)_{T=T_c} = \dfrac{\mu_0 H_a{}^2}{2}, \tag{2.4.4}$$

where $\beta_{GL}(T_c) = \beta_{GLc}$, H_a is apparent magnetic field

Finally, it is a formula about magnetic field dependence of temperature under the

limitation approaching T_c

$$H_c(T) = H_c(0)\left[1 - \left(\dfrac{T}{T_c}\right)^2\right]. \tag{2.4.5}$$

9
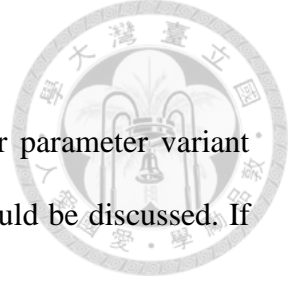
2.4.2　The GL Equation

However, external magnetic field can actually cause the order parameter variant with space. For generation situation, the more complicated case should be discussed. If the order parameter vary with space which means $\psi = \psi\left(\vec{r}\right)$, the extra term in Eq (2.4.1) is

$$\frac{1}{2m^*}\left|\left(\frac{h}{i}\nabla - \frac{e^*}{c}\vec{A}\right)\psi\right|^2 . \tag{2.4.6}$$

To solve this, let $\psi = |\psi|e^{i\varphi}$ and the remaining term can be written as

$$\frac{1}{2m^*}\left|\left(\hbar^2\left(\nabla|\psi|^2\right) + \left(\hbar\nabla\varphi - \frac{e^*}{c}\vec{A}\right)^2|\psi|^2\right)\right|^2 , \tag{2.4.7}$$

where $\vec{B}\left(\vec{r}\right) = \nabla \times A\left(\vec{r}\right)$, $\vec{B}\left(\vec{r}\right)$ is the interior magnetic field. The first term contributes to extra energy associated with gradient. The second term is the kinetic energy with supercurrents in a gauge-invariant form. In this case, Eq (2.4.1) can be rewritten as

$$F_s = F_n + \alpha_{GL}|\psi|^2 + \left(\frac{\beta_{GL}}{2}\right)|\psi|^4 + \frac{1}{2m^*}\left|1 - i\hbar\nabla\psi - -e^*\vec{A}\psi\right|^2 + \frac{1}{2\mu_0}B^2 - \vec{B}\cdot\overline{H_a} . \tag{2.4.8}$$

The GL equation can be obtained by integrating Eq (2..4.7) with ψ and A, respectively.

$$\frac{1}{2m^*}\left(-i\hbar\nabla - e^*\vec{A}\right)^2\psi + \alpha_{GL}\psi + \beta_{GL}|\psi|^2\psi = 0, \tag{2.4.9}$$

with the boundary condition $\vec{n}\cdot\left(-i\hbar\nabla\psi - e\vec{A}\right)\psi = 0$.

$$\frac{1}{\mu_0}\nabla \times \vec{B} = -\frac{\hbar e^*}{2im}\left(\psi^*\nabla\psi - \psi\nabla\psi^*\right) - \frac{e^{*2}}{m}|\psi|^2\vec{A} = \vec{j_s} , \tag{2.4.10}$$

with the boundary condition $\vec{n}\times\left(\frac{\vec{B}}{\mu_0} - \overline{H_a}\right) = 0$. The equation (2.4.9) and (2.4.10) are

10

called first GL equation and second GL equation, respectively. Theoretically, GL equation and Maxwell equation can solve $\psi\left(T,\vec{r},\overline{H}\right)$ and $\vec{A}\left(T,\vec{r}\right)$ in most part of superconductor. However, the general solution is too difficult to deal with so, in general situation, the calculation just be an approximation under different condition.
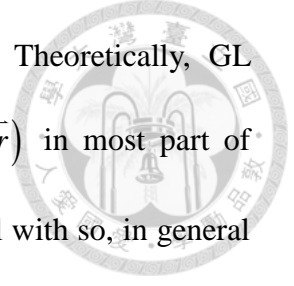
2.4.3   The GL Penetration Depth and Coherence Length

Although the general solution of the GL equation cannot be obtained, the GL equations give the two characteristic length to study superconductor in different types superconductor. Firstly, consider another case of weak magnetic field $H \approx 0$ $\left(\psi \approx \psi_0\right)$ with the sample dimensions much greater than the magnetic penetration depth , the second GL equation becomes

$$\vec{j}_s = -\frac{e^{*2}}{m^*c}\left|\psi_0\right|^2\vec{A}, \tag{2.4.11}$$

taking the curl of both sides and replacing $\left|\psi_0\right|^2 = \dfrac{\left|\alpha_{GL}\right|}{\beta_{GL}}$

$$\nabla\times\vec{j}_s = -\frac{e^{*2}}{m^*c}\left|\psi_0\right|^2\vec{B} = -\frac{e^{*2}}{m^*c}\frac{\left|\alpha_{GL}\right|}{\beta_{GL}}\vec{B}, \tag{2.4.12}$$

substituting $\vec{j}_s = \dfrac{c}{4\pi}\left(\nabla\times\vec{B}\right)$ into Eq (2.4.12)

$$\frac{m^*c^2}{4\pi e^{*2}}\frac{\beta_{GL}}{\left|\alpha_{GL}\right|}\left(\nabla\times\nabla\times\vec{B}\right)+\vec{B} = 0. \tag{2.4.13}$$

Comparing with London equation, the GL penetration depth is given

$$\lambda\left(T\right) = \left(\frac{m^*c^2\beta_{GL}\left(T\right)}{4\pi e^{*2}\left|\alpha_{GL}\left(T\right)\right|}\right)^{1/2}, \tag{2.4.14}$$

11

this result is consistent with London penetration depth if $\left|\psi_0\right|^2 = \dfrac{|\alpha|}{\beta} = n_s^*$. Substituting

Eq (2.4.14) into Eq (2.4.4) get the parameter α_{GL} and β_{GL}

$$\alpha_{GL}(T) = -\frac{e^{*2}}{m^* c^2} H_c^2(T) \lambda^2 , \tag{2.4.15}$$

$$\beta_{GL}(T) = \frac{4\pi e^{*4}}{m^{*2} c^4} H_c^2(T) \lambda^4(T) . \tag{2.4.16}$$

The next case is that assuming ψ varies only in one direction $\hat{z}$ and without external magnetic field. In the case the first GL equation becomes

$$-\frac{\hbar^2}{2m^*} \frac{d^2\psi}{dz^2} + \alpha_{GL}\psi + \beta_{GL}\left|\psi\right|^2 \psi = 0 , \tag{2.4.17}$$

if z is real and introduce a new dimensionless order parameter

$$f(z) = \frac{\psi(z)}{\left|\psi_0\right|} . \tag{2.4.18}$$

The Eq (2.4.17) can be rewritten as

$$-\frac{\hbar^2}{2m^*\left|\alpha_{GL}\right|} \frac{d^2 f(z)}{dz^2} - f(z) + f^3(z) = 0 . \tag{2.4.19}$$

From Eq (2.4.19), a length scale for spatial variation of the order parameter is given by

$$\xi(T) = \left(\frac{\hbar^2}{2m^*\left|\alpha_{GL}(T)\right|}\right)^{1/2} , \tag{2.4.20}$$

which is called the GL coherence length. This two characteristic length are both depend on temperature.
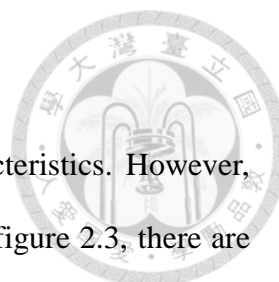
2.5   Type-I and Type-II Superconductor

As pervious mentioned, there are two superconducting characteristics. However, the one of feature is violated in some superconductor. As shown in figure 2.3, there are two different types of superconductor which can be categorized according to their magnetic behaviour.

2.5.1   Magnetization of the Superconductor

A type-I superconductor excludes the whole magnetic field until a critical field H_c. When the magnetic field exceeds the critical field H_c the superconducting state will be destroyed.

A type-II superconductor can also keep the magnetic field outside until the external magnetic field reach the lower critical field H_{c1} and then the magnetic field can enter into the superconductor to form a mixed state. The mixed state means that there are both superconducting state and normal state inside. With increasing magnetic field until upper critical magnetic field H_{c2}, the superconducting state will be completely broken.
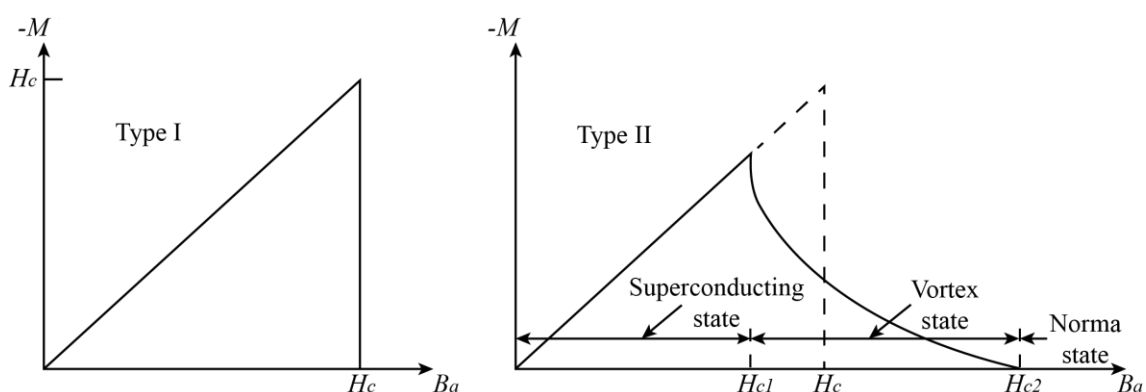
Figure 2.3 Magnetization M versus applied magnetic field H for Type-I and Type-II superconductor.

The magnetic field can enter into superconductor in the form of vortex which is surrounded by superconducting current due to Cooper pair motion and the magnetic flux is quantized. The magnetic flux Φ in the vortex is integral multiple of magnetism quantum flux ϕ_0.

$$\Phi = n\phi_0, \tag{2.5.1}$$

where n is positive integer and ϕ_0 is superconducting magnetic flux quantum with

$\phi_0 = \dfrac{h}{2e}$.

The radius of vortex is determined by coherence length. As shown in figure 2.4, the magnetic field in the center is equal to external magnetic field and exponentially decay from the core with the decay length which is equal to penetration depth. The lower and upper critical field are also determined by the penetration length and coherence length, respectively.

$$H_{c1}(T) = \frac{\Phi_0}{4\pi\lambda^2(T)}, \tag{2.5.2}$$

$$H_{c2}(T) = \frac{\Phi_0}{2\pi\xi^2(T)}. \tag{2.5.3}$$

14
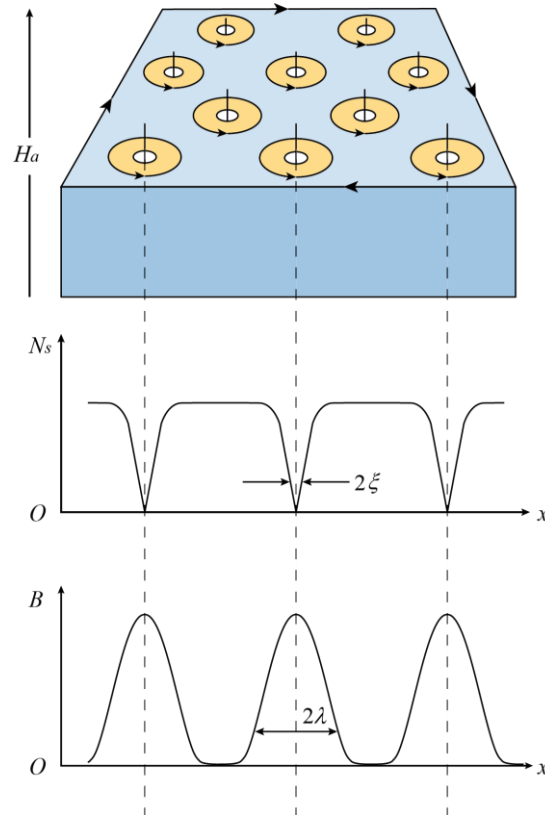
Figure 2.4 Mixed state of Type-II superconductor

2.5.2 Dimensionless GL Parameter κ

It is known that there are two types of superconductor which can be distinguished by a dimensionless parameter which is so-called GL parameter κ. In the GL theory, there are two characteristic lengths coherence ξ and penetration length λ. By using these two characteristic lengths, define a dimensionless GL parameter κ by

$$\kappa \equiv \frac{\lambda(T)}{\xi(T)}, \tag{2.5.4}$$

this parameter can be used to distinguish two different types of superconductor by [14].

$$\begin{cases} \kappa < \dfrac{1}{\sqrt{2}}, & \text{Type I} \\[2mm] \kappa > \dfrac{1}{\sqrt{2}}, & \text{Type II} \end{cases}, \tag{2.5.5}$$

15
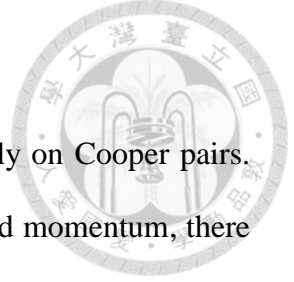
2.6   Upper Critical Field Limits

Conventional superconductor is described by BCS which is rely on Cooper pairs. Because Cooper pairs consist of two electrons with opposite spin and momentum, there are two limitations of upper critical magnetic field which are contributed to two different ways which can possible break Cooper pairs in the presence of an external magnetic field. The first one is orbital limit due to the Lorentz force. The second one is spin paramagnetic limit result from Zeeman effect.

In [15],   Werthamer, Helfand and Honenberg (WHH) studied the temperature and purity dependence of the critical field. The temperature dependence of magnetic field and spin-orbit scattering can be expressed

$$\ln\frac{1}{t} = \left(\frac{1}{2} + \frac{i\lambda_{SO}}{4\gamma}\right)\psi\left(\frac{1}{2} + \frac{\hbar + \frac{1}{2}\lambda_{SO} + i\gamma}{2t}\right) + \left(\frac{1}{2} - \frac{i\lambda_{SO}}{4\gamma}\right)\psi\left(\frac{1}{2} + \frac{\hbar + \frac{1}{2}\lambda_{SO} - i\gamma}{2t}\right) - \psi\left(\frac{1}{2}\right), \quad (2.6.1)$$

where $t = \dfrac{T}{T_c}$, $\gamma \equiv \left[\left(\alpha_{Maki}\hbar\right)^2 - \left(\frac{1}{2}\lambda_{SO}\right)^2\right]^{1/2}$, $\hbar = -\dfrac{4\mu_0 H_{c2}}{\pi^2\left(\dfrac{dH_{c2}}{dt}\right)_{t=1}}$, $\alpha_{Maki} = \dfrac{\sqrt{2}H_{c2}^{orb}(0)}{H^P(0)}$

and ψ is digamma function. Eq (2.6.5) consider both the orbit limit and the spin limit. α_{Maki} is so-called Maki parameter which can be used to determine which effect dominate the upper critical magnetic field limit, orbit limit or spin limit. λ_{SO} is a parameter describing the strength of spin-orbit scattering. With WHH theory, Eq (2.6.5) can be used to analyze the experimental result by adjusting the parameter λ_{SO} and α_{Maki}.
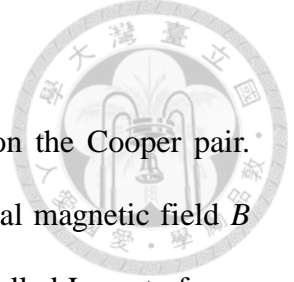
2.6.1 Orbital Limit

The orbital pair breaking is due to the Lorentz force acting on the Cooper pair. According to general physics, when an electron moves in an external magnetic field B or electric field with the velocity V_e, it will suffer a force which is called Lorentz force. In the superconductor, it can just be considered the case without electric field so the Lorentz force can be written as

$$F_{Lorentz} = BeV_e , \qquad (2.6.2)$$

where B is external magnetic field, e is the charge and V_e is the velocity of electron.

The original centripetal force [16], which form the Cooper pair, is

$$F_c = \frac{\Delta}{\xi_0} , \qquad (2.6.3)$$

where $\Delta = \dfrac{\hbar V_e}{2\xi_0}$ is the superconducting energy gap and ξ_0 is the minima coherence.
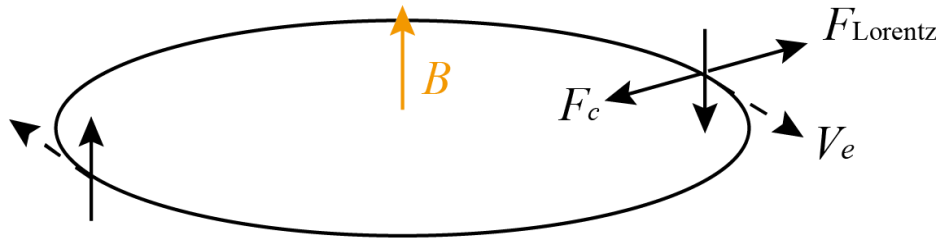

Figure 2.5 Lorentz force act on the Cooper pair and break the superconducting state.

To keep the superconducting state, these two forces must satisfy

$$\frac{\Delta}{\xi_0} \geq BeV_e , \qquad (2.6.4)$$

under the limit condition,

$$B_{c2} \leq \frac{\phi_0}{2\pi\xi_0^2} . \qquad (2.6.5)$$

Eq (2.6.5) represents the orbital limit of upper critical magnetic field.

17

In WHH theory with the absence of spin effect $(\alpha_{Maki} = 0)$, the upper critical is restricted by orbit limit. The Eq (2.6.1) can be rewritten as simple one

$$\ln\frac{1}{t} = \psi\left(\frac{1}{2} + \frac{\hbar}{2t}\right) - \psi\left(\frac{1}{2}\right),$$

(2.6.6)

and then the upper critical magnetic field of orbit limit can be derived as

$$\mu_0 H_{c2}^{orb}(0) = -0.69T_c\left(\frac{d\mu_0 H_{c2}}{dT}\right)_{T=T_c},$$

(2.6.7)

where μ_0 is vacuum permeability and T_c is the critical temperature.

2.6.2 Spin Paramagnetic Limit

The spin paramagnetic limit results from the Zeeman effect which align the spin of two electrons of Cooper pair with direction of external magnetic field [17, 18]. Zeeman effect is that, with an external magnetic field, the electron orbital momentum and the spin momentum will couple and induce energy splitting. When the spin polarization energy exceeds the superconducting condensation energy, the superconducting behavior will be suppressed. According to the BCS theory, the energy gap at $T = 0$ is $\Delta(0) = 1.76k_B T_c$ [5]. The polarization energy is $\frac{1}{2}\chi_n H_P^2$ where $\chi_n = \frac{g^2\mu_B^2 N(0)}{4}$ is the magnetic susceptibility and μ_B is Bohr magneton and $N(0)$ is the density of state on the Fermi surface.
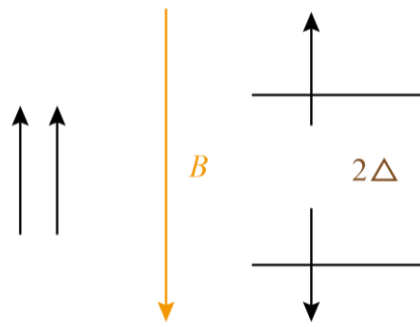
18

Figure 2.6 The spin paramagnetic limit due to the Zeeman effect.

The spin limit can be calculated by the equilibrium of these two energy

$$\frac{1}{2}\chi_n H_P^2 = N(0)\frac{\Delta^2}{2}. \tag{2.6.8}$$

Substituting $\Delta = 1.76k_B T$, $\chi_n = \dfrac{g^2\mu_B^2 N(0)}{4}$ and $g = 2$ (for free electron) into Eq

(2.6.8), the Pauli paramagnetic limit can be expressed by

$$H_P = 1.85T_c. \tag{2.6.9}$$

The spin paramagnetic can be possibly enhanced in the case of strong electron-phonon coupling, spin-orbital coupling or pairing state [19].

2.7   Spin-orbit Interaction

2.7.1   Spin-orbit interaction

The electrons can be thought of a spinning charge ball and the correlated angular momentum is spin. The interaction of the electron spin with the electric field which is related magnetic field in the electrons rest frame with the lattice motion is so-called spin-orbit interaction.

19

2.7.2 Elliot-Yafet mechanism

There are different mechanisms to explain spin-orbit interaction. The Elliot-Yafet (EY) mechanism is generally used to explain spin-orbit interaction in Al. Elliott propose that spin-orbit interaction will cause different wave function from all band mixed so electron momentum change in the process of momentum relaxation which means that the spin-orbit scattering can flip the spin of electron. If the EY mechanism lead the scattering mechanism, the momentum scattering time is proportional to the spin relaxation time [20].
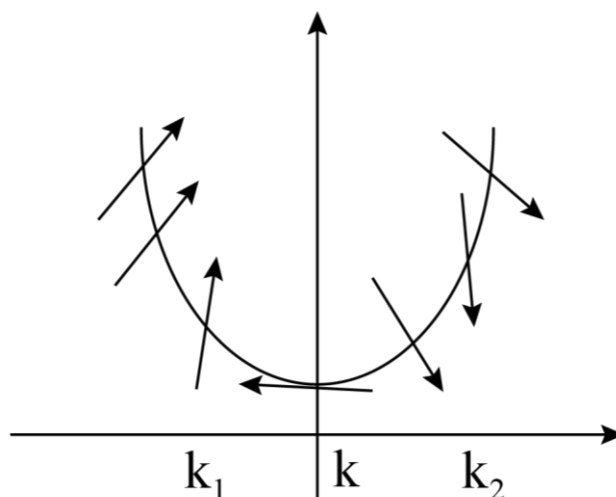

Figure 2.7 Spin polarizations at different wavevector.

The spin-orbit interaction can play a role in superconductivity. Previously our group have already studied this effect and show that with the decreasing thickness the spin-orbit interaction can be strong which is indicated by the decreasing spin-orbit relaxation time and it also consistent with the results of this thesis [21].

2.8   BKT Transition

The Berezinskii-Kosterlitz-Thouless (BKT) transition is a topological transition in 2D system. This topological transition is related to topological charge excitation process. In superconducting state, vortex and anti-vortex can be seemed as topological charged. In a 2D superconducting system vortex-antivortex pairs which is bound at low temperatures would dissociate into free vortices at a characteristic transition Temperature T_{BKT}. Because the ordered state has power law decay and the disordered state has exponential decay, by electronic properties measurement, an easy way to find the BKT transition is to observe the relation between voltage and current. The BKT transition occurs where $V \sim I^3$ [22-25]. Our group member have already showed the BKT transition in Al with different methods and the results are consistent with each other [26].

21
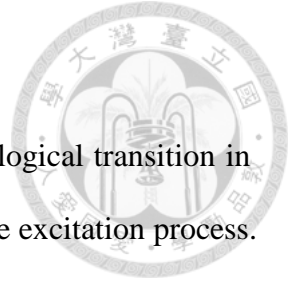
REFERENCES

[1]   H. K. Onnes, *Leiden Comm.* (1911).

[2]   W. Meissner and R. Ochsenfeld, *Naturwiss,* 21, 787 (1933).

[3]   C. J. Gorter and H. B. G. Casimir, *Phys*, 1, 306 (1934a)

[4]   F. London and H. London, *Proc. R. Soc.*, A, 155, 71 (1935).

[5]   J. Bardeen, L. N. Cooper and J. R. Schrieffer, *Phys. Rev.* 108, 5 (1957).

[6]   J. Bardeen, L. N. Cooper and J. R. Schrieffer, *Phys. Rev.* 106, 162 (1957).

[7]   Leon Cooper, *Phys. Rev.* 104, 1189 (1956).

[8]   Alan M. J. Kadin, *Supercond. Nov. Mag*. 20(4), 285 (2005)

[9]   Shigeji Fujita; Kei Ito; and Slavador Godoy, (2009). *Quantum Theory of Conducting Matter*. Springer Publishing. pp. 15–27.

[10]   Richard P. Feynman, Robert Leighton; and Matthew Sands. *Lectures on Physics, Vol.3. Addison–Wesley*. pp. 21–7, 8. (1965)

[11]   W. S. Corak, B. B. Goodman, C. B. Satterthwaite, and A. Wexler, *Phys. Rev.* 102, 656 (1956).

[12]   V. L. Ginzburg and L. D. Landau, *J. Exp. Theor. Phys.* (USSR) 20, 1064 (1950).

[13]   L. P. Gor'kov Sov. *Phys. JETP* 36, 6 (1959)

[14]   A. A. Abrikosov, *J. Exp. Theor. Phys.* (USSR) 32, 1442 (1957).

[15]   N. R. Werthamer, E. Helfand and P. C. Honenberg, *Phys. Rev.* 147, 295 (1966))

[16]   http://web.mit.edu/6.763/www/FT03/Lectures/Lecture17.pdf

[17]   A. M. Clogston, *Phys. Rev. Lett.* 9, 6 (1962).

[18]   B. S. Chandrasekhat, *Appl. Phys. Lett.* 1, 1 (1962).

[19]   J. L. Zhang, L. Jiao, Y. Chen, H. Q. Yuan, *Phys. Condens. Matter.* 6, 463 (2012).

[20] R. J. Elliott *Phys. Re.* 96 266 (1954).

[21] S.-T. Lo, S.-W. Lin, Y.-T. Wang, S.-D. Lin and C.-T. Liang, *Sci. Rep.* 4, 5438 (2014).

[22] A. F. Hebard and A. T. Fiory, *Phys. Rev. Lett.* 44, 291 (1980).

[23] N. D. Mermin and H. Wanger, *Phys. Rev. Lett.* 17, 1307 (1966).

[24] M. R. Beasley, J. E. Mooij and T. P. Orlando, *Phys. Rev. Lett.* 42, 1165 (1979).

[25] D. S. Fisher, M. P. Fisher, and D. A. Huse, *Phys. Rev. B* 43, 1130 (1991).

[26] Guan-Ming Su, "Studies of Kosterlitz–Thouless Transition: Numeric Simulation of the 2D XY Model and 2D Superconductivity in 4-nm Aluminum Nano-Film," M.S. thesis, National Taiwan University, Taiwan, 2018.

Chapter 3   Device fabrication and Measurement Technique

This chapter will cover the device fabrication and measurement technique. The aluminum (Al) films were prepared by Prof. Sheng-Di Lin's group at NCTU using molecular beam epitaxy (MBE) system. The measurement was performed by Prof. Chi-Te Liang's group at NTU using a cryo-free He^3/He^4 dilution refrigerator.

3.1   Device Fabrication

In this section, I will briefly introduce the concept of MBE and the fabrication process of the device. The detailed growth processes can be found in Ref. [1].

3.1.1   Molecular-beam Epitaxy

The MBE technique was developed by Arthur and Cho in 1960s at Bell Laboratories [2]. It is usually used to grow nanostructure device with controllable thickness and high quality. Under the condition of ultra-high vacuum, by heating up the material to sublime, the gaseous elements will condense on substrate. The atoms condense on surface of substrate slowly and systematically in ultra-thin layer. The quality was mainly influenced by deposition rate which is tuned by temperature and pressure.

3.1.2　Fabrication Processes

The fabrication processes can be divided into three parts. First, the substrate was baked for cleaning the surface. The second part is growing Al by MBE. Finally, the device was shaped into a Hall-bar for electrical property measurement.
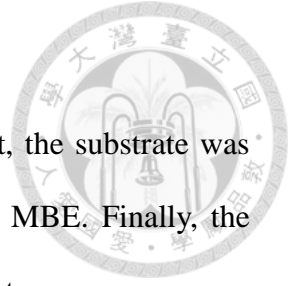
(i)　Baking substrate:

As shown in figure 3.1, there are three stages of this process for removing the steam, organic and oxidized layer respectively. The substrate was baked for 8 hours at 200 °C and then backed for 5 hours at 400 °C, and finally baked for 20 minutes at 600 °C.
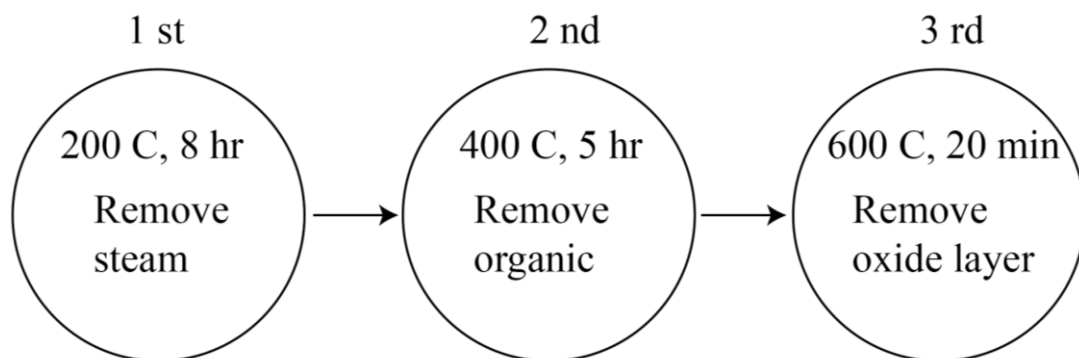

Figure 3.1 Baking substrate process.

(ii)　Growing Al:

Under the condition of Ga-rich, the Al nanofilm can be grown with high quality and flat surface. For this purpose, the substrate was grown a 200-nm-thick undoped GaAs buffer layer at 580 °C and then heated up to 600 °C without arsenic flux to transform the surface into Ga-rich condition for 3 minutes. After that, the sample was cooled down and subsequently Al was grown on the surface at the rate of 0.1 nm/s.

(iii) Hall-bar fabrication

For electrical measurements, Al nanofilms were shaped into Hall-bar by photolithography. The fabrication started with exposure, followed by development which was using TMAH developer to shape the Hall-bar. Next, the exposure and the development which was using AZ developer was applied again to form the pad and then using E-gun deposited 200 nm thick Al layer to protect Al etched by followed procedure and then grown Al_2O_3 with atomic layer deposition (ALD) to form passivation. The last step was using BOE etching on the region of pad and depositing Ti and Au of 20 nm and 200 nm respectively for contact.

The size of device was shown in figure 3.2 with the length of device is 1630 μm × 1020 μm and the width of Hall-bar are 100 μm and 40 μm. The OM image is shown in figure 3.3-3.5 for 3-nm-thick, 3.5-nm-thick and 4-nm-thick, respectively.
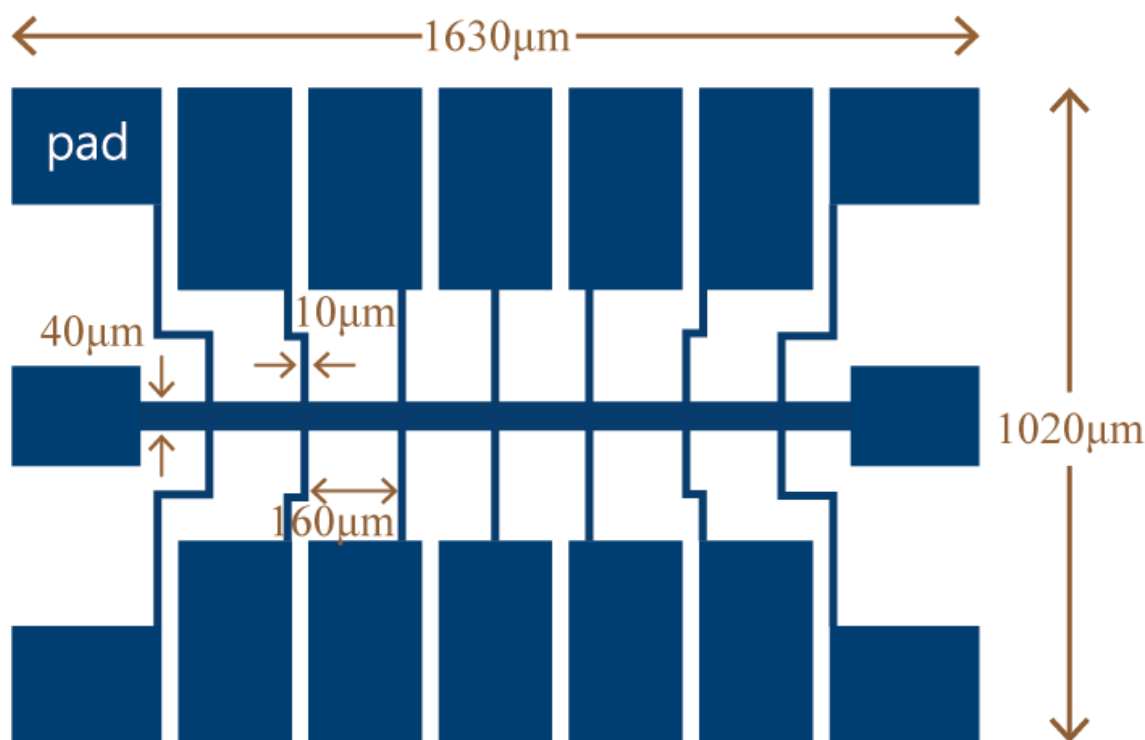

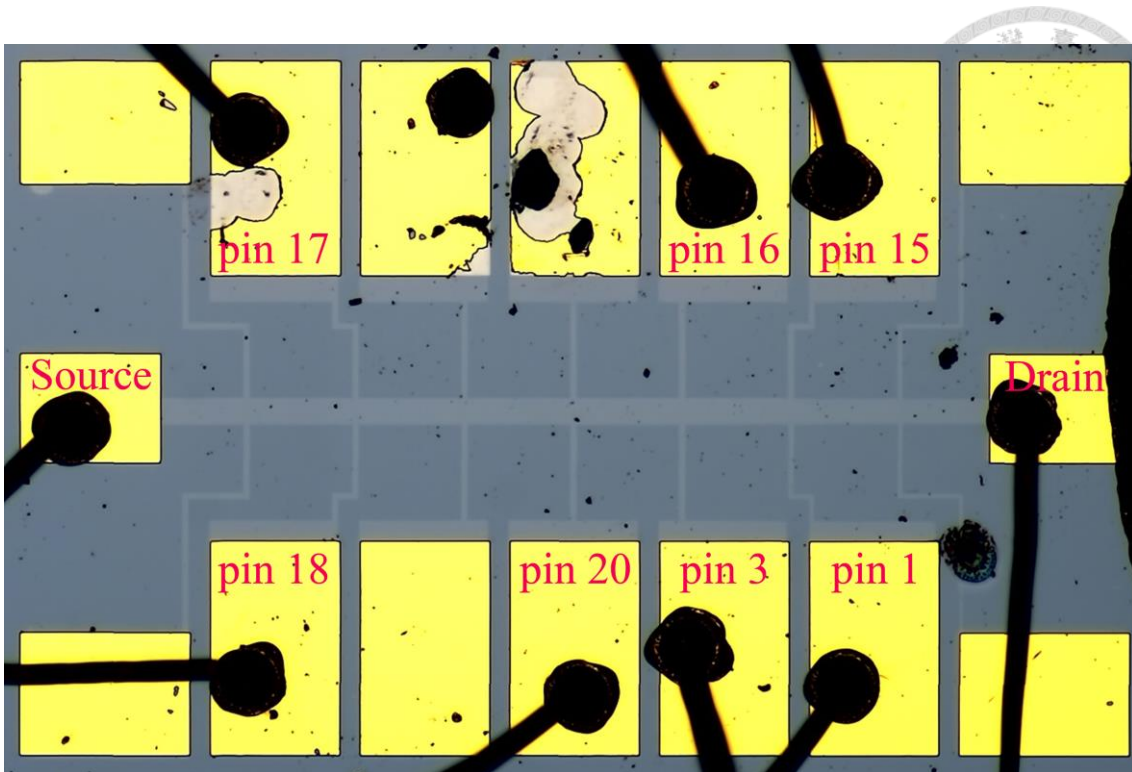Figure 3.2 schematic diagram of device.
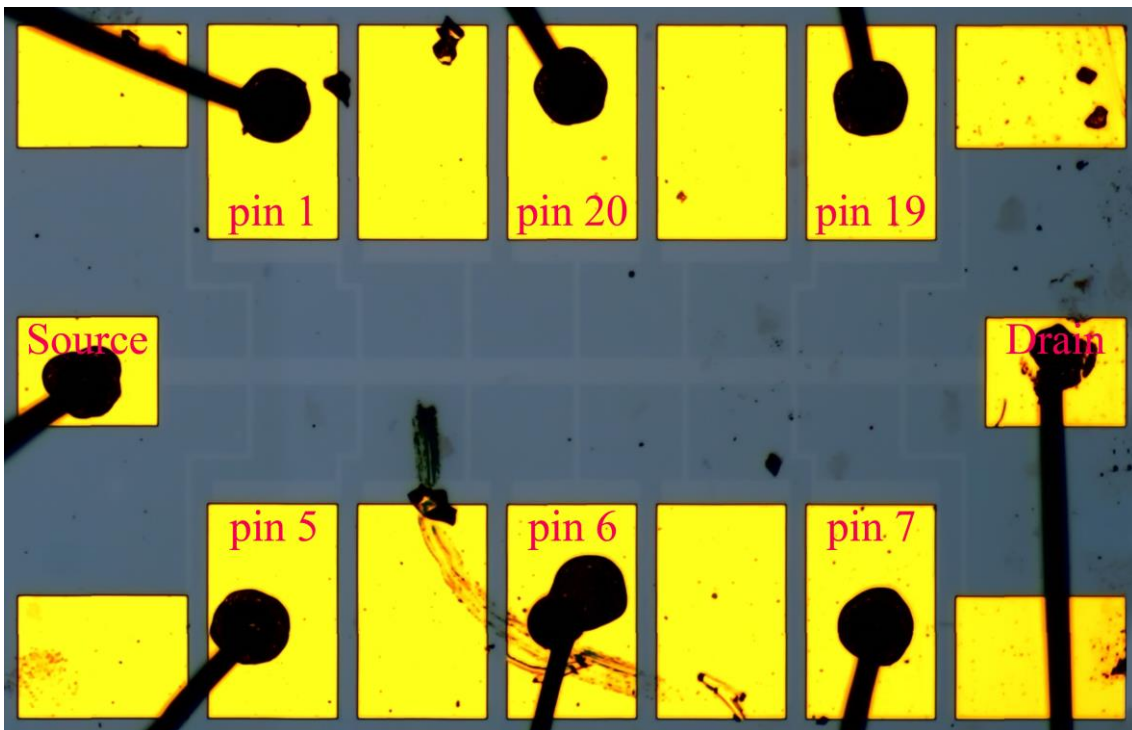
26

Figure 3.3 OM image of 3-nm-thick device.

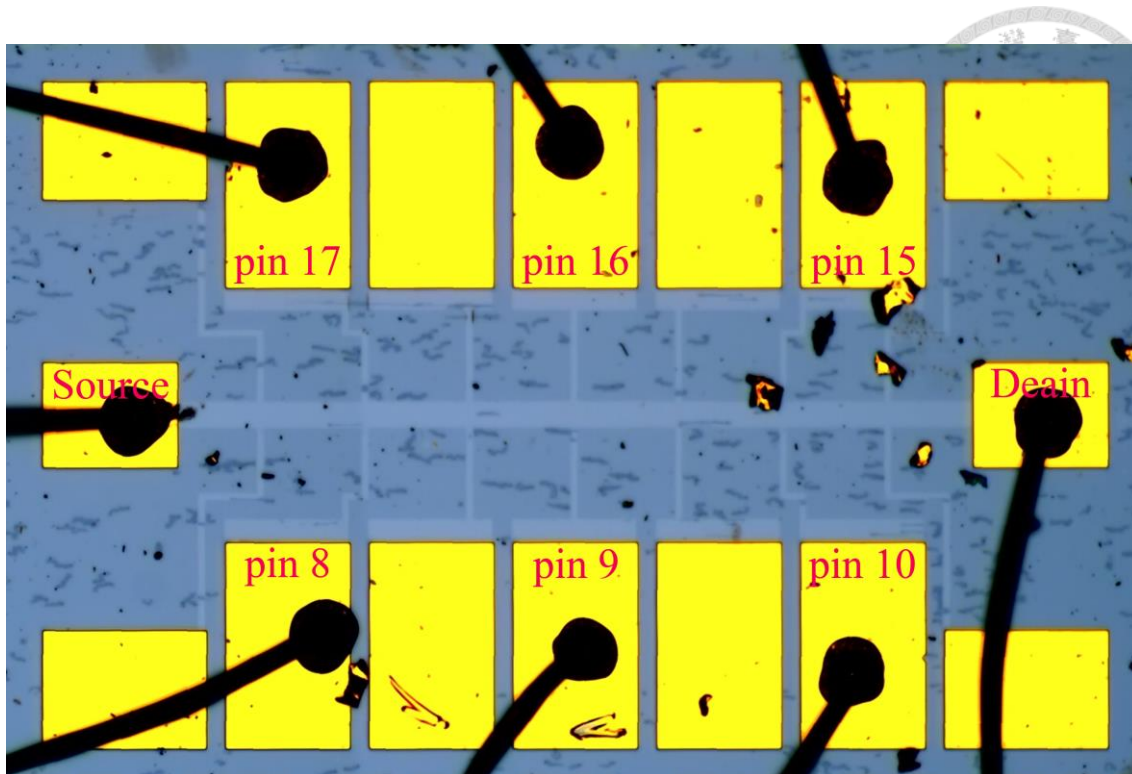Figure 3.4 OM image of 3.5-nm-thick device.

Figure 3.5 OM image of 4-nm-thick device.

3.2   Low-temperature System

The experiments were performed in an Oxford Triton 200 cryo-free He^3/He^4 dilution refrigerator. The dilution refrigerator is a cryogenic system which can cold down to around 20 mK. The concept was proposed by Heinz London in early 1950s and realized in 1964 [3]. The mechanism relies on thermodynamic characteristics of the mixture of two isotopes of He^3 and He^4. As shown in figure 3.6, when cooled below a critical temperature (about 870 mK) the mixture is spontaneously separated into two liquid phase which is divided by a phase boundary. The working fluid is He^3 which is circulated by vacuum pumps. When the He^3 moves from the He^3-rich phase (right of triple point) to the He^4-rich phase (left of the triple point), it expand and take heat out of the chamber and then reduce the temperature.
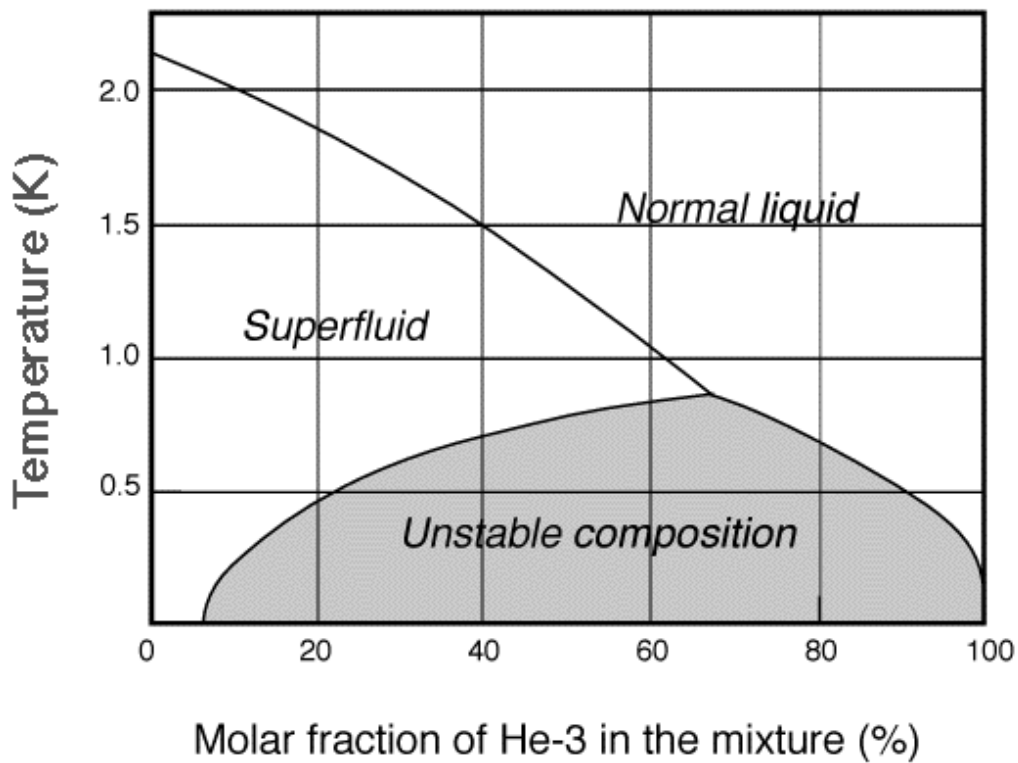
28

Figure 3.6 The phase diagram of He^3 and He^4 mixture.(Take from [4])

3.3　　Four-terminal DC Measurements

Standard four-terminal dc resistance measurements were performed on the devices. As shown in figure 3.7, the device's source was connected to a Keithley 2400 multi-meter which providing a current from source to drain. The voltage drops between each voltage probes was measured by Keithley 2000 multi-meter.

The advantage of using four-terminal measurement is that the influence of contact resistance can be diminished.
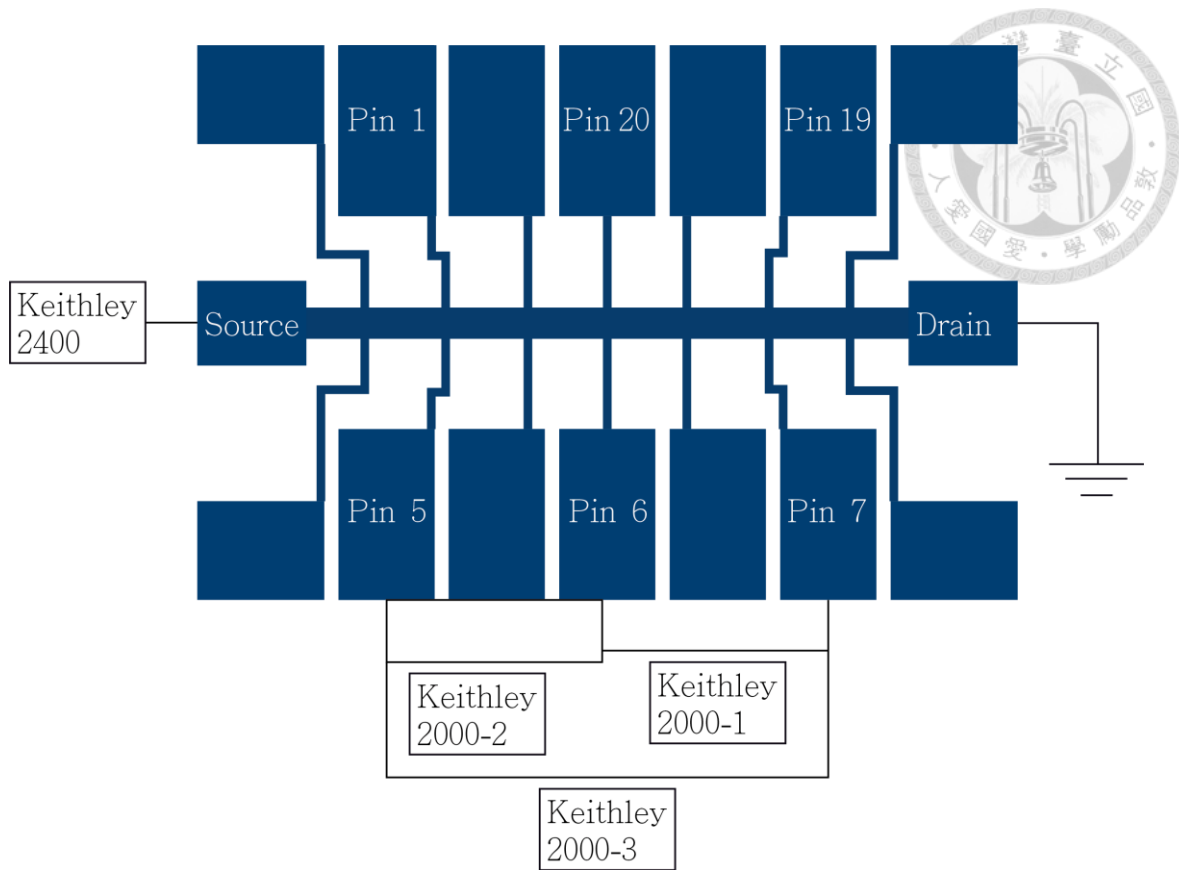
29

Figure 3.7 The schematic of four-terminal measurement of 3.5-nm-thick device.

REFERENCES

[1]   Y.-T. Fan, M.-C. Lo, C.-C. Wu, P.-Y. Chen, J.-S. Wu, C.-T. Liang, and S.-D. Lin, *AIP Adv*. 7, 075213 (2017).

[2]   A. Y. Cho and J. R. Arthur *Prog. Solid State Chem*. 10, 157 (1975).

[3]   P. Das R. Bruyn de Ouboter, and K. W. Taconis. *A Realization of a London-Clarke-Mendoza Type Refrigerator*.

[4]   http://ltl.tkk.fi/research/theory/mixture.html

Chapter 4   Results and Discussion

Four-terminal dc measurement was performed on our devices which are of different thickness (3-nm-thick, 3.5-nm-thick and 4-nm-thick) to measure the current-voltage (*I-V*) curves. The process and correlated machine is mentioned in Chapter 3.
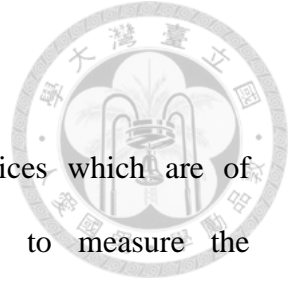
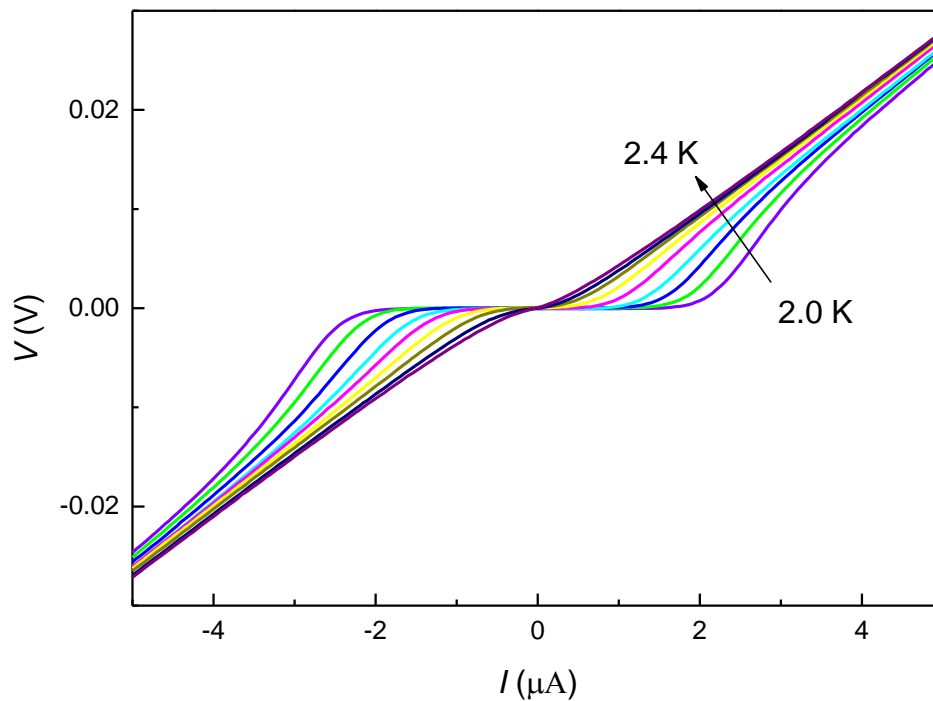## 4.1   Electronic Properties of MBE-Grown Al Nanofilms

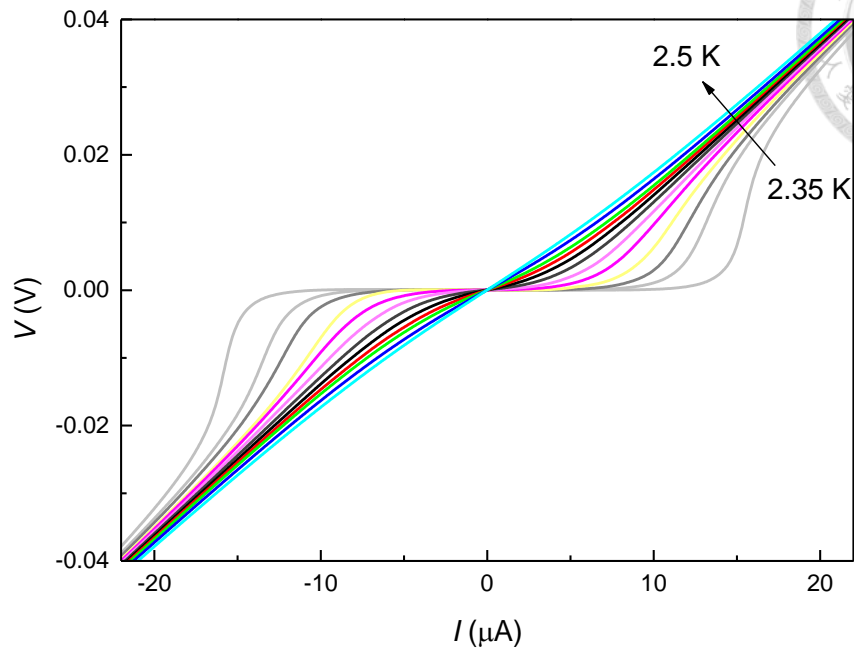Figure 4.1 *I-V* curves of the 3-nm-thick Al nanofilm at various temperatures.

Figure 4.2 *I-V* curves of the 3.5-nm-thick Al nanofilm at various temperatures.
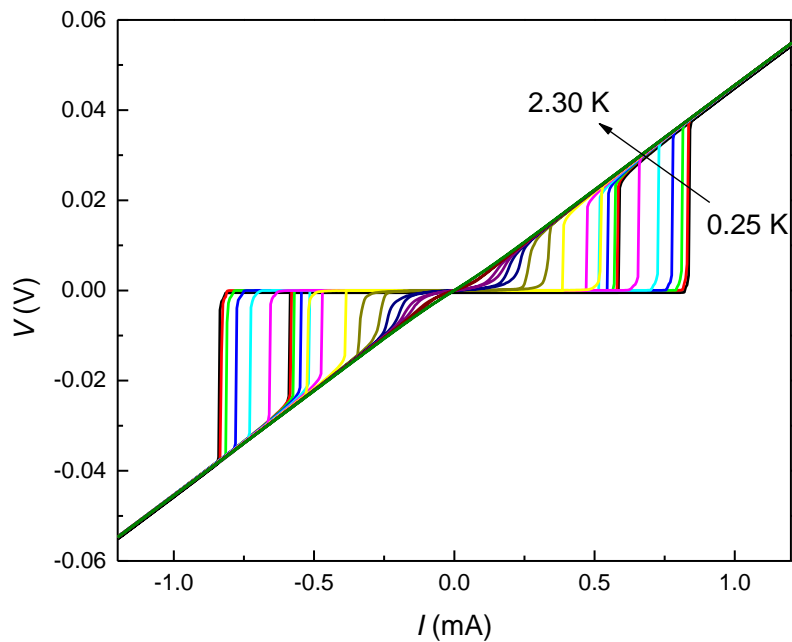

Figure 4.3 *I-V* curves of the 4-nm-thick Al nanofilm at various temperatures.

33

Figures 4.1-4.3 show *I-V* characteristics of the 3-nm, 3.5-nm and 4-nm-thick Al nanofilms at different temperatures, respectively. When the temperature is lower than the critical temperature and the current is lower than the critical current, our samples show the zero-resistance state which is a superconducting behavior. The transition is sharp which indicate good quality of Al nanofilm and I define the critical current at the certain point which it shows an abrupt change to the normal state at the lowest temperature (0.25 K). At lowest temperature 0.25 K, the critical currents are 13.6 μA, 64.55 μA, and 820 μA for the 3-nm-thick, 3.5-nm-thick, and 4-nm-thick samples, respectively.
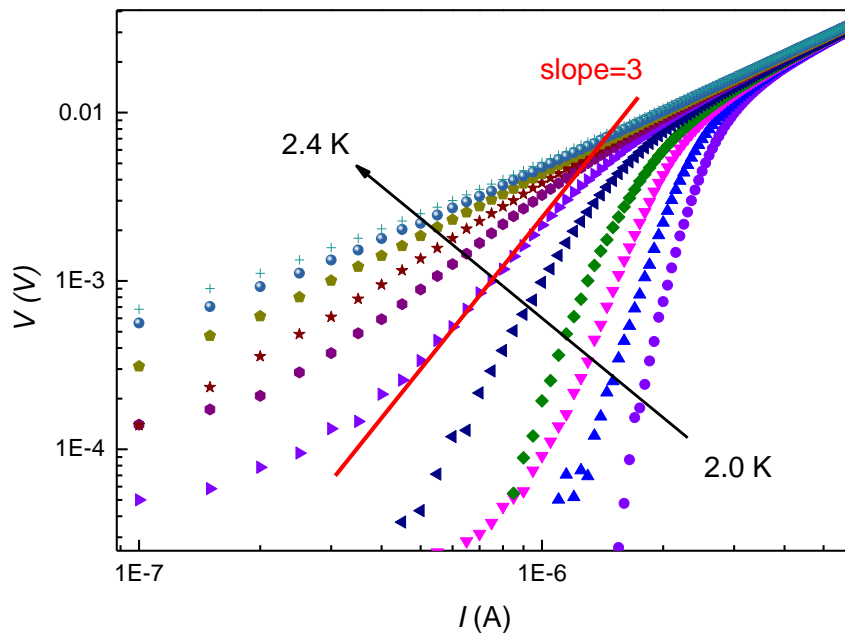

Figure 4.4 *I-V* curves of the 3-nm-thick device for various temperatures on a log-log scale. The black straight line corresponds to $V \sim I^3$.
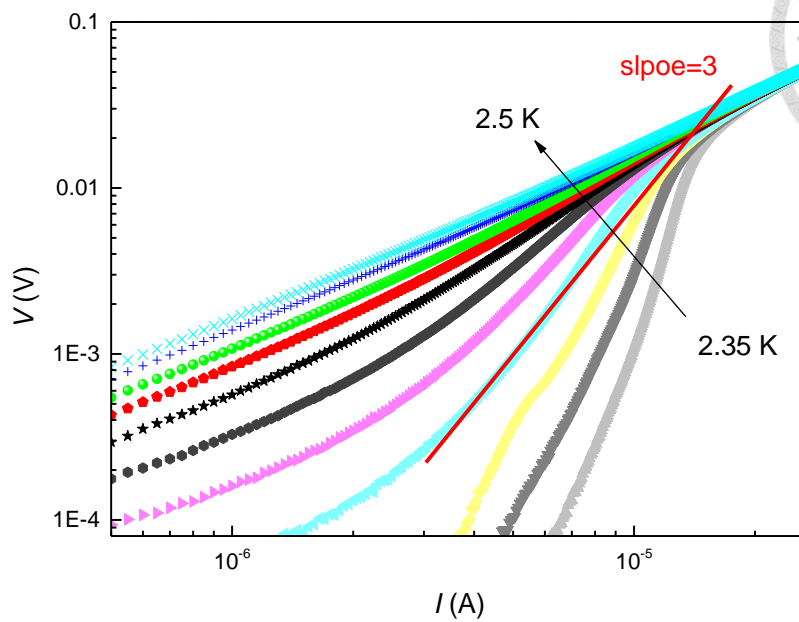
34

Figure 4.5 *I-V* curves of the 3.5-nm-thick device for various temperatures on a log-log

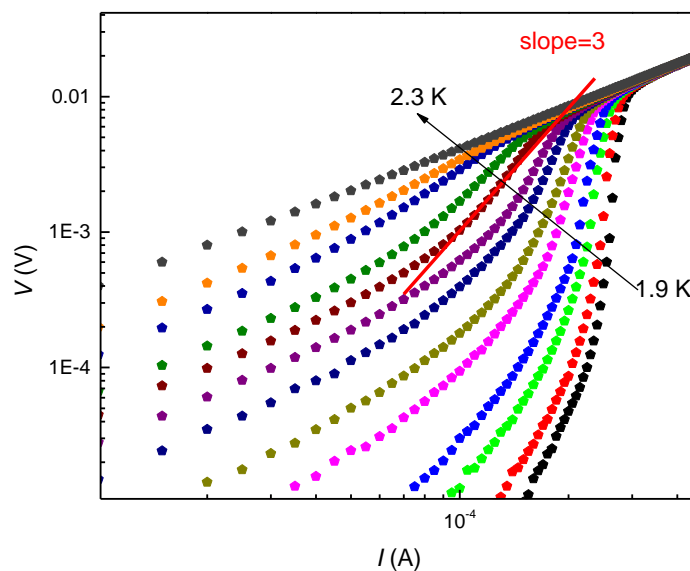scale. The black straight line corresponds to $V \sim I^3$.

Figure 4.6 *I-V* curves of the 4-nm-thick device for various temperatures on a log-log

scale. The black straight line corresponds to $V \sim I^3$.

The data shown in figures 4.4-4.6 are extracted from figures 4.1-4.3. In these figures, the *I-V* curves was plotted at different temperatures on a log-log scale. The red line with slope 3 was drawn to find when the BKT transition take place. The linear fit was applied to find the slope α $\left(V \sim I^{\alpha} \right)$ at each temperature and the temperature dependence of the exponent α is plotted in figures 4.7-4.9. The BKT transition temperature will be determined when find where the slope of the fit is 3.
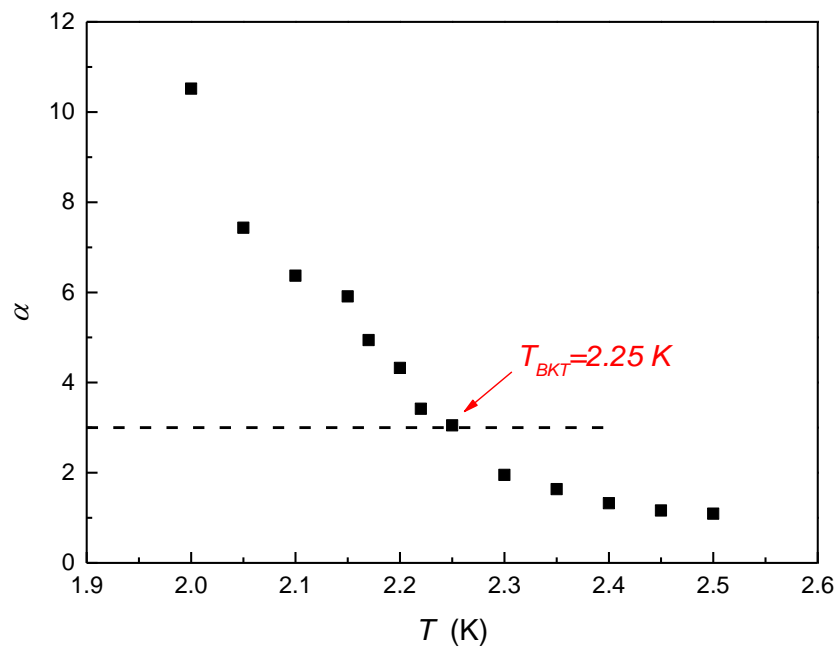

Figure 4.7 *α*(*T*) obtained on the 3-nm-thick device. The data are extracted from those shown in figure 4.4.
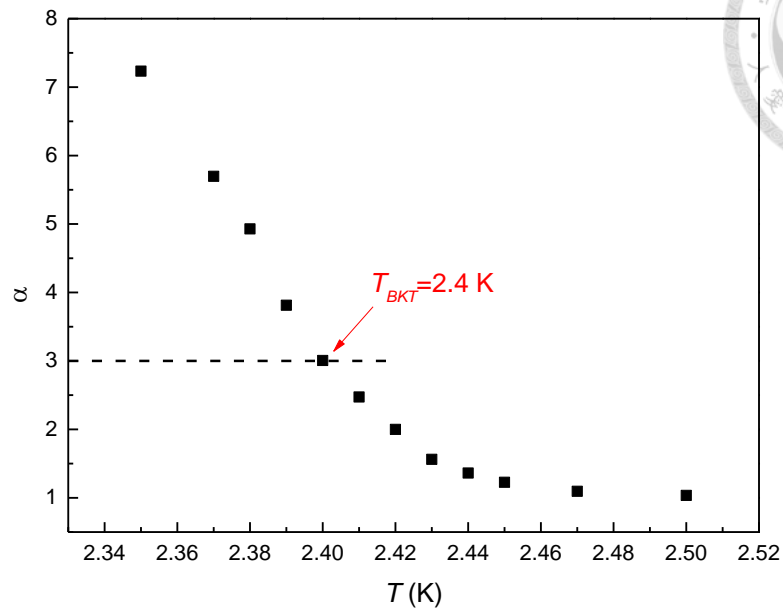
36

Figure 4.8 $\alpha(T)$ obtained on the 3.5-nm-thick device. The data are extracted from those shown in figure 4.5.
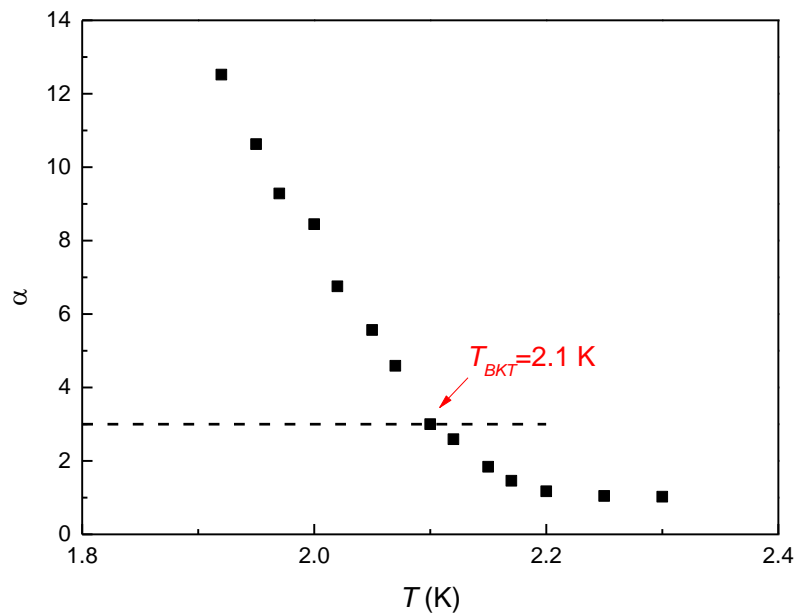

Figure 4.9 $\alpha(T)$ obtained on the 4-nm-thick device. The data are extracted from those shown in figure 4.6.

37

In figures 4.7-4.9, the slope at temperature was found. At where the slope is 3 indicate the BKT transition occurring. At higher temperatures, the slope is 1 which indicates the metallic behavior. The BKT transition temperature (T_{BKT}) of the 3-nm, 3.5-nm and 4-nm thick films are 2.25 K, 2.4 K and 2.1 K, respectively.
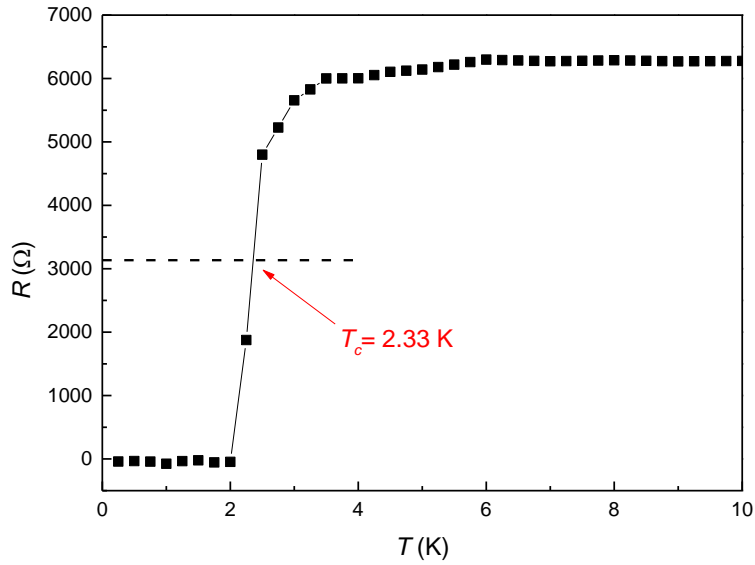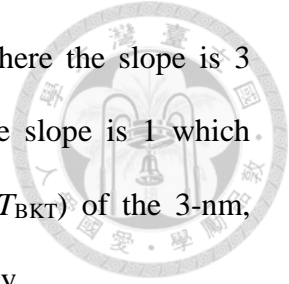

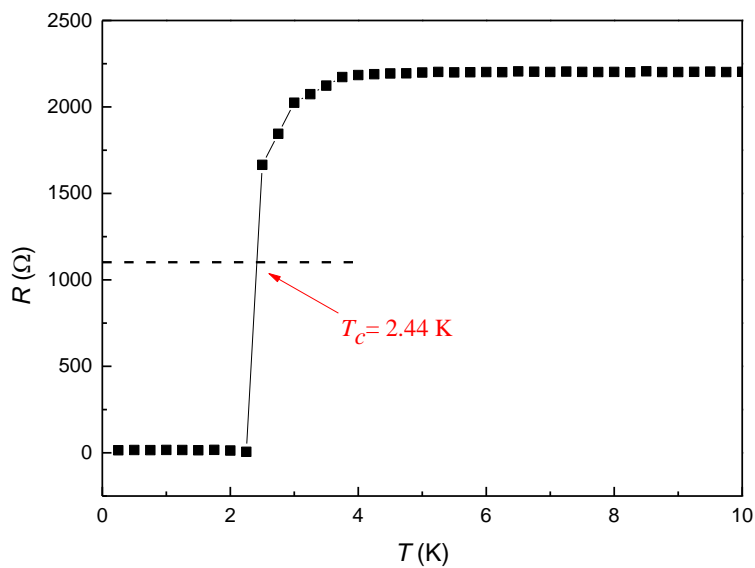Figure 4.10 *R-T* curve of the 3-nm-thick device.

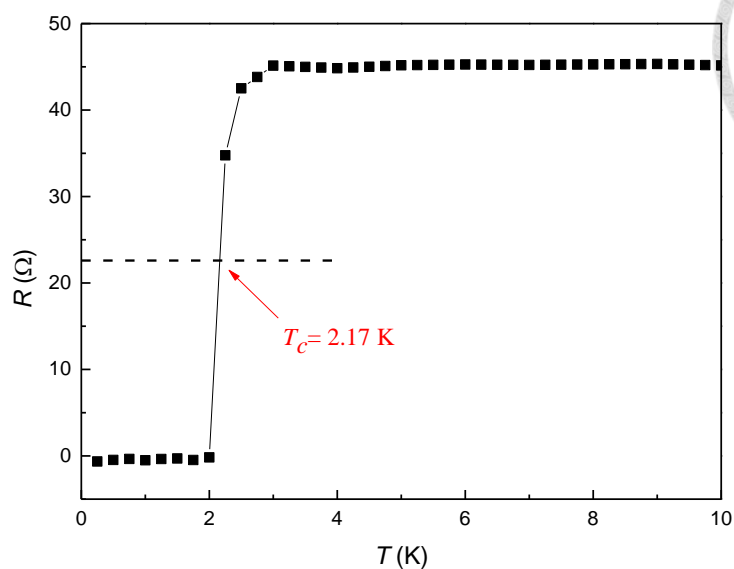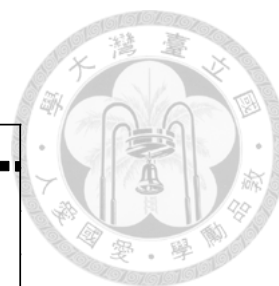Figure 4.11 *R-T* curve of the 3.5-nm-thick device.

38

Figure 4.12 *R-T* curve of the 4-nm-thick device.

The resistance dependence of temperature is shown in figures 4.9-4.12 by applying a constant current and measuring the resistance at different temperatures. The critical temperature is chosen at the temperature where the resistance is half resistance of the saturating value in the normal state. The critical temperature (T_c) of each films are 2.33 K, 2.44 K and 2.17 K respectively. It is acceptable that the critical temperatures are slightly higher than BKT transition temperatures. When temperature lower than the critical temperature the Al nanofilms become superconductor and then vortex and anti-vortex appear in interior of superconductor. The superconductor changes from disorder state to order state.

39

Thickness (nm)	3	3.5	4
Critical Current I_c (μA)	13.6	64.55	820
BKT Transition T_{BKT} (K)	2.25	2.4	2.1
Critical Temperature T_c (K)	2.33	2.44	2.17

Table 4-1 Key parameters for samples with different thicknesses.

4.2 Magneto-transport in MBE-Grown Al Nanofilms
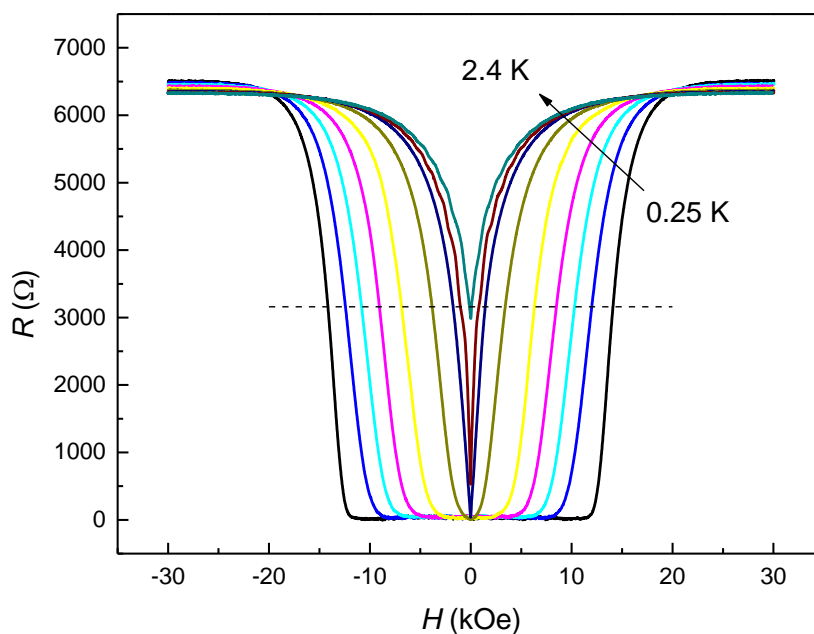

Figure 4.13 $R(H)$ data taken on the 3-nm-thick device with H perpendicular to the plane of film at different temperatures.

40
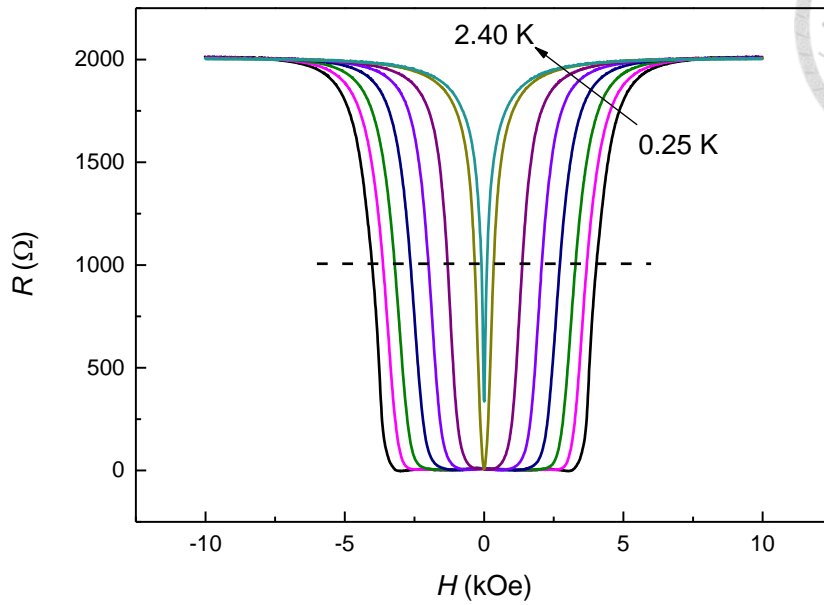
Figure 4.14 R(H) data taken on the 3.5-nm-thick device with H perpendicular to the plane of film at different temperatures
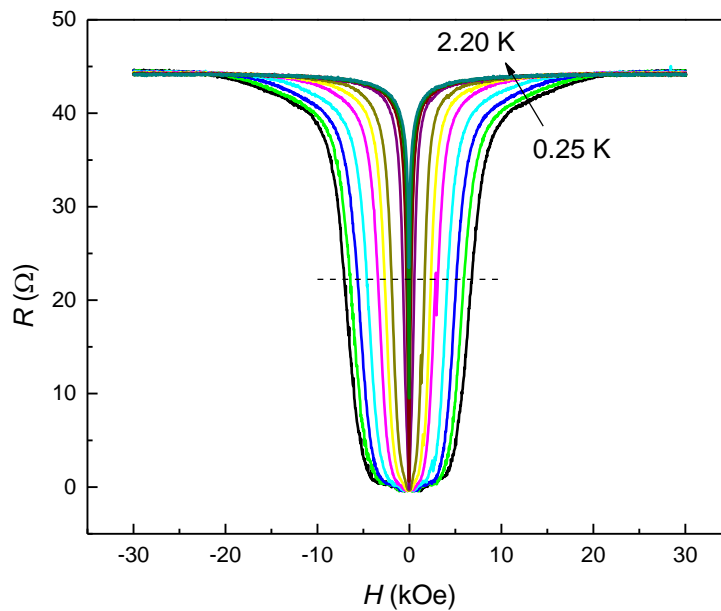

Figure 4.15 R(H) data taken on the 4-nm-thick device with H perpendicular to the plane of film at different temperatures

41

Figures 4.13-4.15 show the resistance dependence of the magnetic field which is perpendicular to the films dependence, the data was measured by applying a constant current and sweeping the magnetic field which is perpendicular to the film simultaneously with measuring the resistance. Because the *H-R* curves are unlike the *I-V* curves which show a sharp transition, which may indicate a mixed state in transition process, the critical magnetic field was chosen at magnetic field where the resistance is half resistance of the saturating value in a normal state at each temperature.
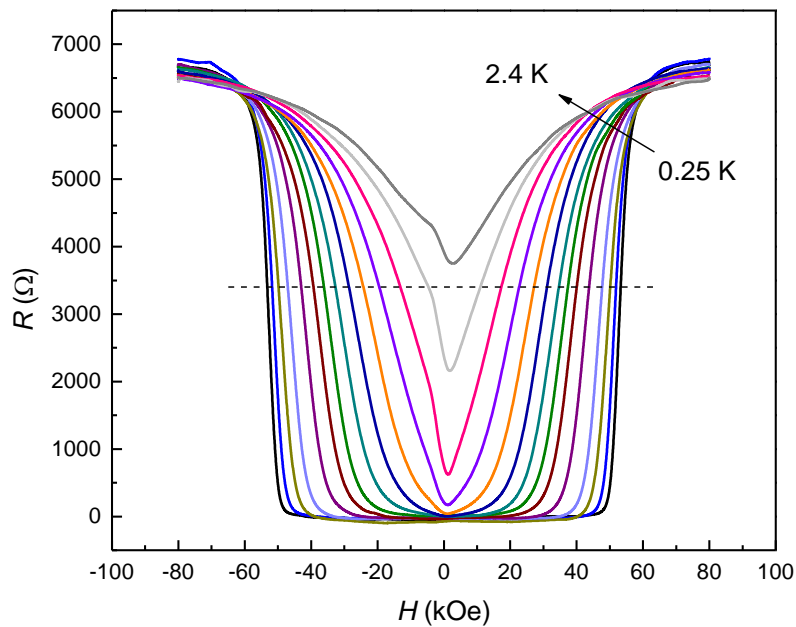

Figure 4.16 *R*(*H*) data taken on the 3-nm-thick device with *H* parallel to the film at different temperatures.
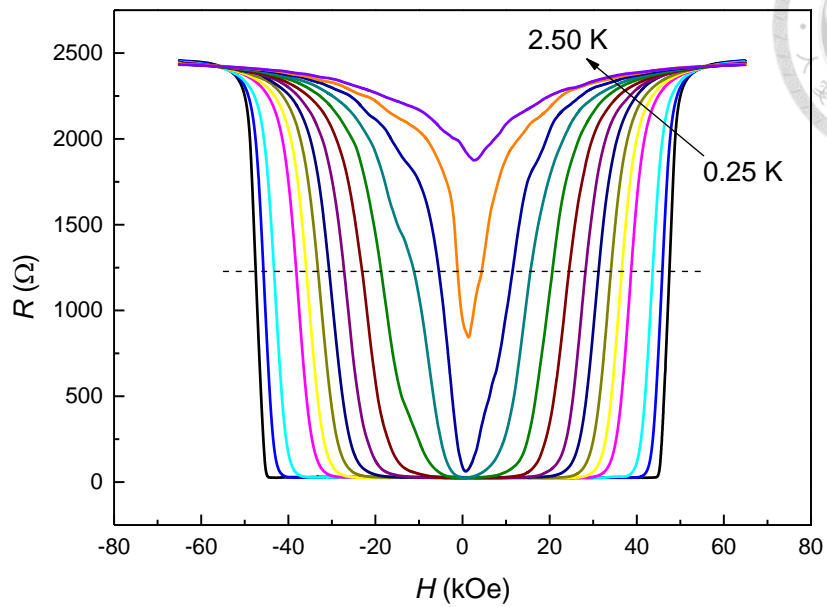
Figure 4.17 *R(H)* data taken on the 3.5-nm-thick device with *H* parallel to the film at different temperatures.
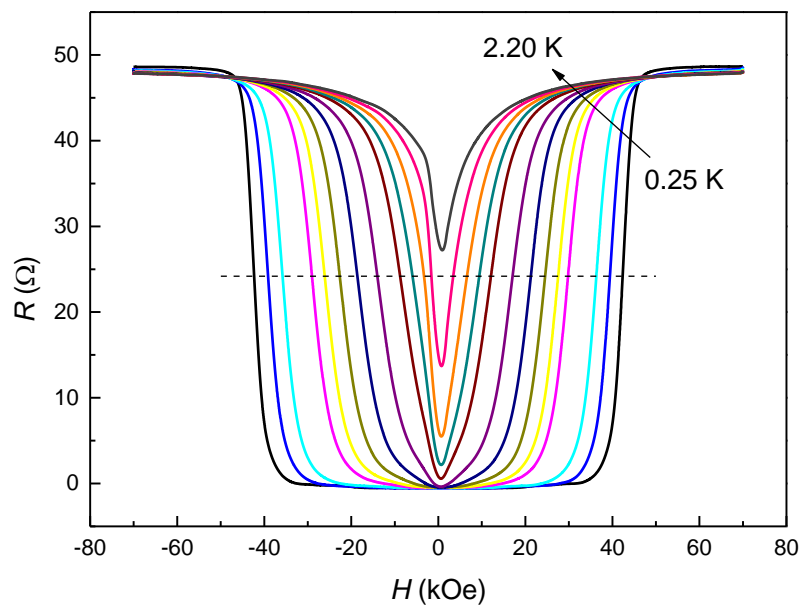

Figure 4.18 *R(H)* data taken on the 4-nm-thick device with *H* parallel to the film at different temperatures.

43

Figures 4.16-4.17 show the resistance dependence of magnetic field which is parallel to the films dependence. The data was measured by the same process as mentioned above in perpendicular magnetic field. Obviously, the parallel critical magnetic field is much higher than the perpendicular critical magnetic field.
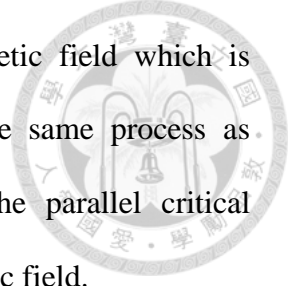
4.3　Analysis and Discussion

With the critical temperature of Al nanofilms are higher than that conventional bulk aluminum which may be contributed to the strain [1, 2].

According to the GL theory, the critical magnetic field as a function of temperature is given by Eq (2.4.5) [3]

$$H_c(T) = H_c(0)\left[1 - (T/T_c)^2\right].$$

(4.3.1)

On the other hand, the parallel critical magnetic field as a function of temperature can be empirically fitted to the following equation [4]

$$H_c(T) = H_c(0)\left[1 - (T/T_c)\right]^{1/2}.$$

(4.3.2)

The Pauli limit, estimated on the basis of the BCS theory $\Delta = 1.78k_BT_c$ is given by Eq (2.6.9) [5, 6]

$$H_p = 18.5T_c \text{<kOe>}.$$

(4.3.3)

44

Figure 4.19 $H_c(T)$ data taken on the 3-nm-thick device. The black squares represent the data taken when a parallel magnetic field is applied to the film and red circles represent the data taken when a perpendicular magnetic field is applied to the plane of the film. The blue curve correspond to fit $H_c(T) = H_c(0)\left[1 - (T/T_c)^2\right]$ and the green curve corresponds to a fit to $H_c(T) = H_c(0)\left[1 - (T/T_c)\right]^{1/2}$. The dashed line indicates the Pauli limit at zero temperature.
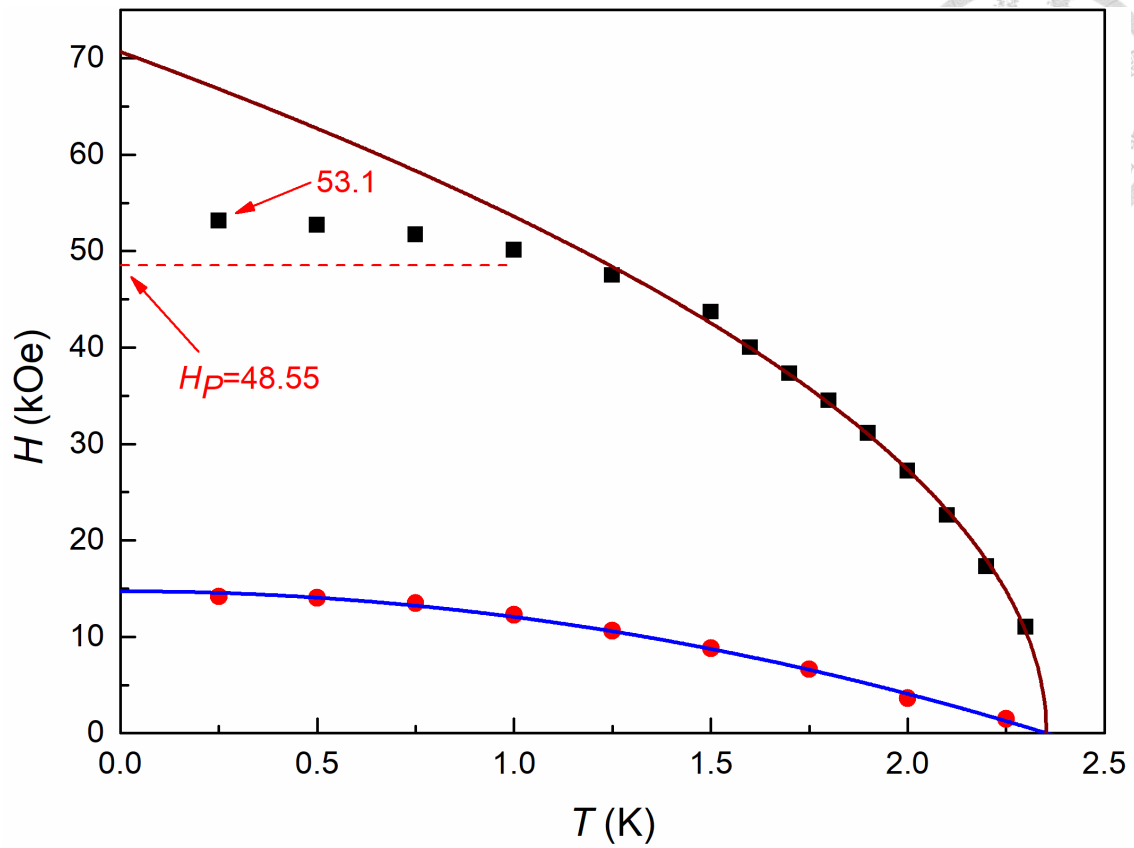
45
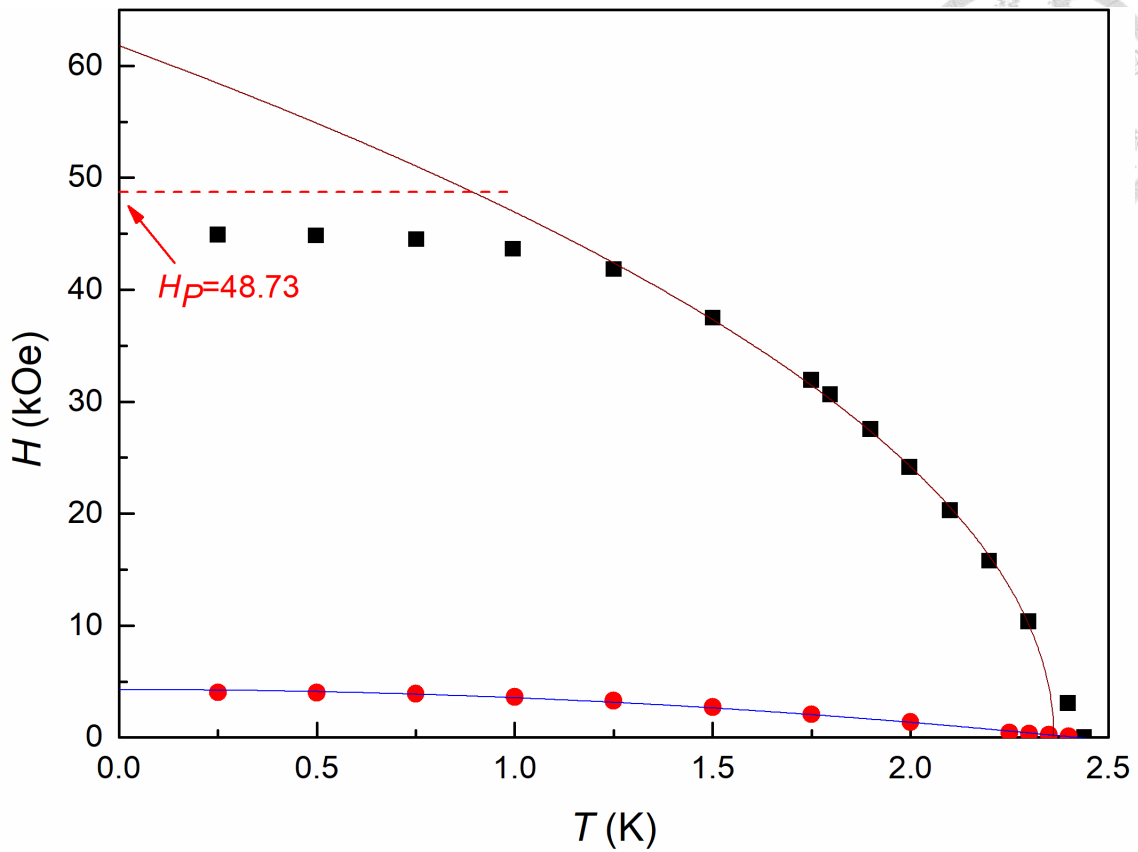
Figure 4.20 $H_c(T)$ data taken on the 3.5-nm-thick device. The Black squares represent the data taken when a parallel magnetic field is applied to the film and red circles represent the data taken when a perpendicular magnetic field is applied to the plane of the film. The blue curve correspond to fit $H_c(T) = H_c(0)\left[1-(T/T_c)^2\right]$ and the green curve corresponds to a fit to $H_c(T) = H_c(0)\left[1-(T/T_c)\right]^{1/2}$. The dashed line indicates the Pauli limit at zero temperature.

Figure 4.21 $H_c(T)$ data taken on the 4-nm-thick device. The Black squares represent the data taken when a parallel magnetic field is applied to the film and red circles represent the data taken when a perpendicular magnetic field is applied to the plane of the film. The blue curve correspond to fit $H_c(T) = H_c(0)\left[1-(T/T_c)^2\right]$ and the green curve corresponds to a fit to $H_c(T) = H_c(0)\left[1-(T/T_c)\right]^{1/2}$. The dashed line indicates the Pauli limit at zero temperature.
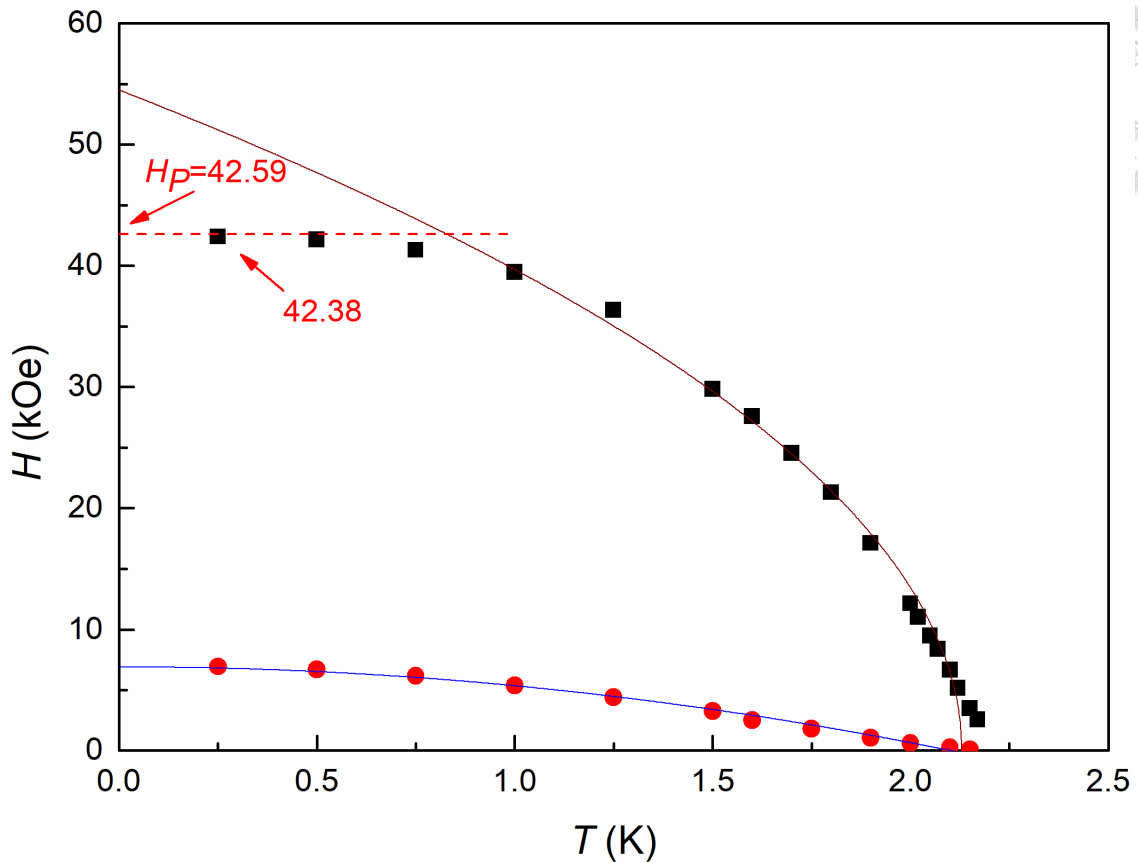
Figure 4.21-4.23 show the $H_c(T)$ curves. Obviously, parallel critical magnetic field is higher than perpendicular. In all cases, the blue curves fit well with all points and brown curves can just fit well in the high temperature region which is because the Eq (4.3.1) is approximation of $T \rightarrow T_c$.

47

In [4], they provide another formula to fit the data and analyze the relation between upper critical magnetic field and spin-orbit scattering by

$$\ln\left(\frac{T}{T_c}\right) + \psi\left(\frac{1}{2} + \frac{\alpha_{pb}}{2\pi T}\right) - \psi\left(\frac{1}{2}\right) = 0,$$

(4.3.4)

where $\alpha_{pb} = \varepsilon + \frac{3}{2}\tau_{SO}\frac{(\mu_B H)^2}{\hbar}$ is a parameter of pair breaking and τ_{SO} is spin-orbit relaxation time. The result is shown in figure 4.22-4.24.
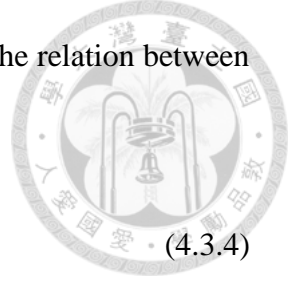

Figure 4.22 $H_c(T)$ data taken on the 3-nm-thick device. The black circles represent the data taken when a parallel magnetic field is applied to the film. The red curve corresponds to the fit $\ln\left(\frac{T}{T_c}\right) + \psi\left(\frac{1}{2} + \frac{\alpha_{pb}}{2\pi T}\right) - \psi\left(\frac{1}{2}\right) = 0$ and the blue curve corresponds to the fit $H_c(T) = H_c(0)\left[1 - (T/T_c)\right]^{1/2}$.

48

Figure 4.23 $H_c(T)$ data taken on the 3.5-nm-thick device. The black circles represent the data taken when a parallel magnetic field is applied to the film. The red curve corresponds to the fit $\ln\left(\dfrac{T}{T_c}\right)+\psi\left(\dfrac{1}{2}+\dfrac{\alpha_{pb}}{2\pi T}\right)-\psi\left(\dfrac{1}{2}\right)=0$ and the blue curve corresponds to the fit $H_c(T)=H_c(0)\left[1-(T/T_c)\right]^{1/2}$.
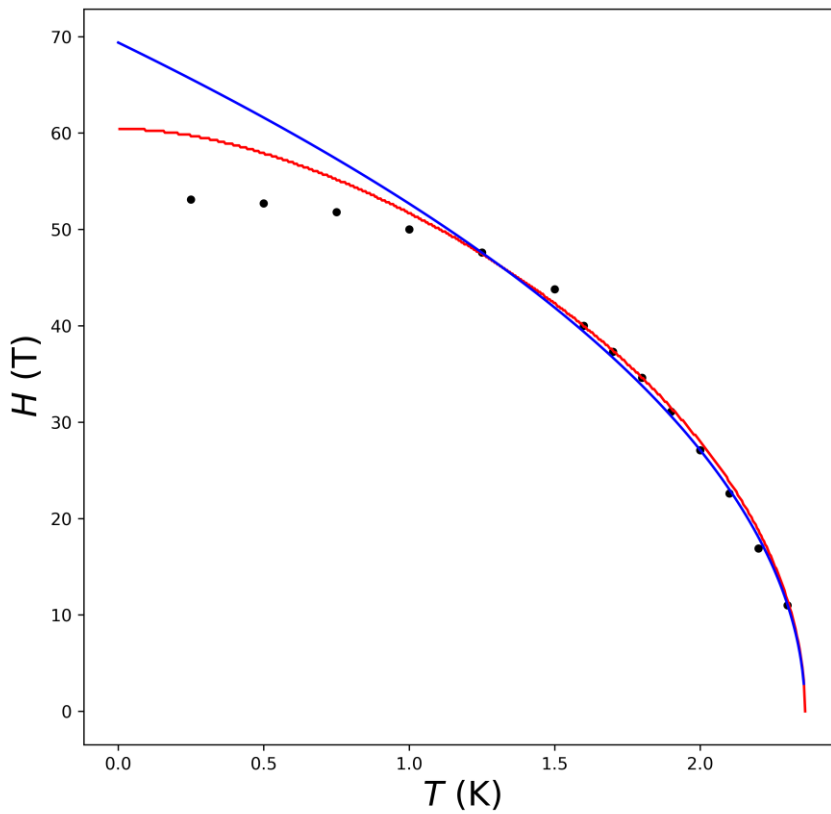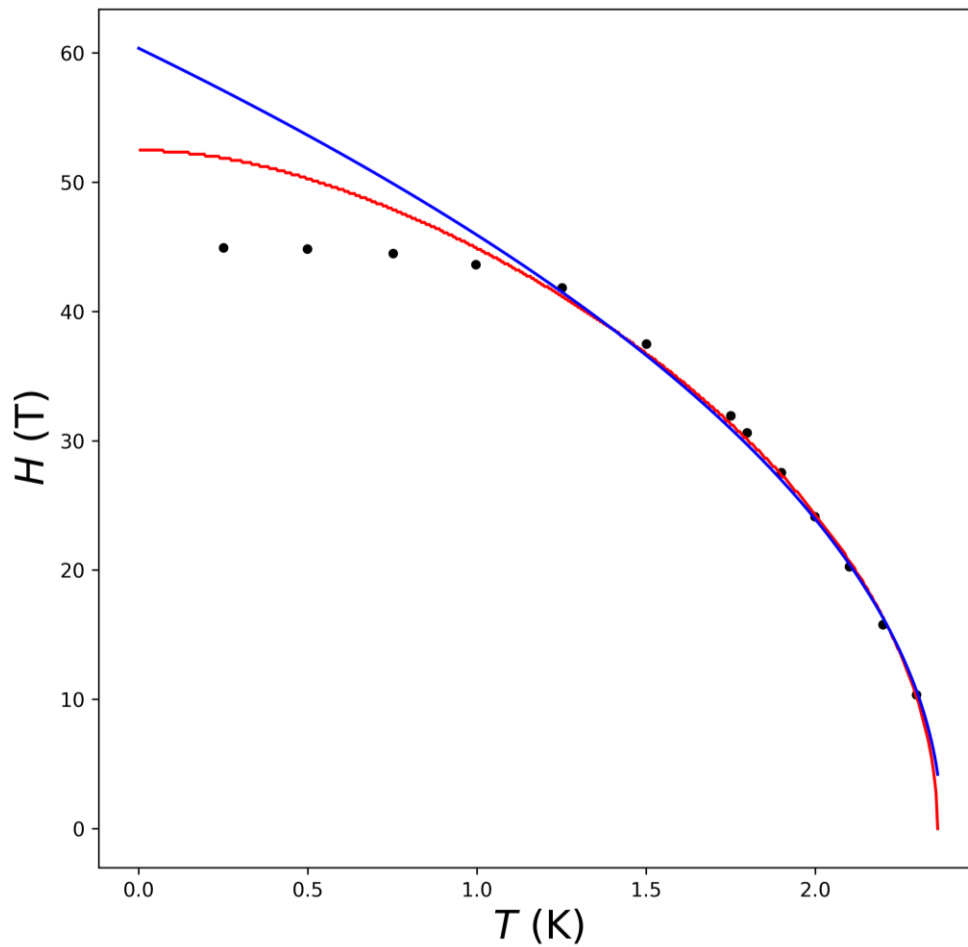
Figure 4.24 $H_c(T)$ data taken on the 4-nm-thick device. The black circles represent the data taken when a parallel magnetic field is applied to the film. The red curve corresponds to the fit $\ln\left(\dfrac{T}{T_c}\right) + \psi\left(\dfrac{1}{2} + \dfrac{\alpha_{pb}}{2\pi T}\right) - \psi\left(\dfrac{1}{2}\right) = 0$ and the blue curve corresponds to the fit $H_c(T) = H_c(0)\left[1 - (T/T_c)\right]^{1/2}$.
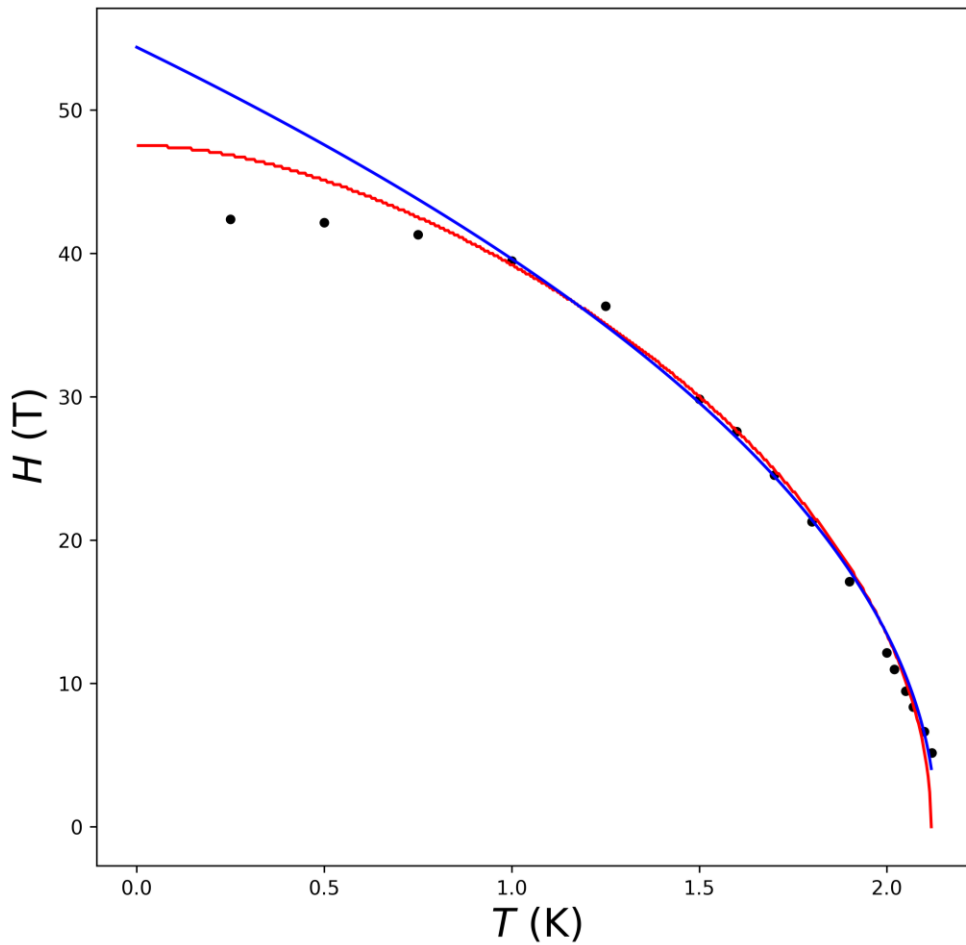
The fit to Eq (4.3.4) is better than that to Eq (4.3.2) at low temperatures. According to the fit, we have the parameter τ_{SO} dependence of thickness.
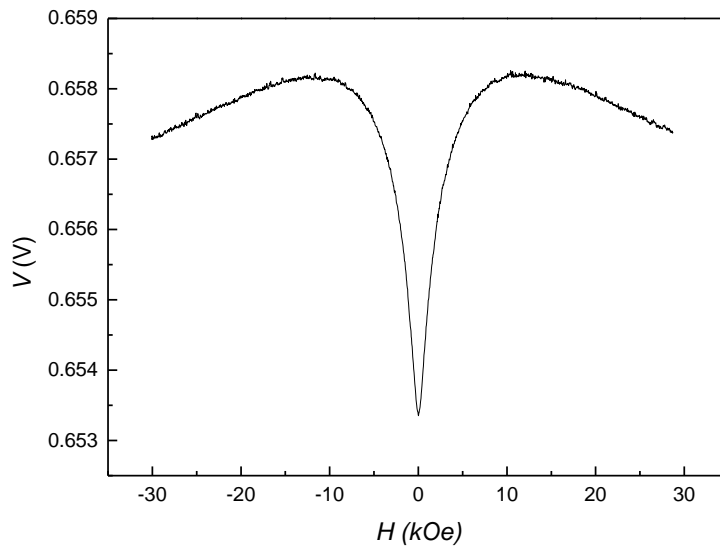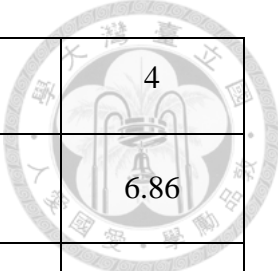
Figure 4.25 H-V_{xx} curves of 3-nm-thick device.

With Hall measurement, figure 4.27 weak anti-localization (WAL) effect. According to the WAL theory developed by Hikami, Larkin and Nagaoka, which assumes that the EY mechanism is responsible for spin-orbit interaction.

Table 4-2 summarizes the measured perpendicular critical magnetic field, parallel critical magnetic field, critical temperature, the Pauli paramagnetic limit, and the spin-orbit relaxation time for all the devices. We can see that in the 3-nm-thick Al film, the parallel magnetic field exceeds the Pauli paramagnetic limit and with decreasing thickness, the spin-orbit relaxation time increase. We interpret this as evidence for spin-orbit coupling in Al superconducting film. In [7], they show that the spin-orbital scattering time τ_{so} decrease with decreasing thickness. Therefore we suggest the Elliott-Yafet mechanism is the dominant mechanism for spin-orbit effect in our Al nanofilms [8].

51

| Thickness (nm)	3	3.5	4
Perpendicular Critical Field $H_{c0+\perp}$ (kOe)	14.80	4.29	6.86
Parallel Critical Field $H_{c0\parallel}$ (kOe)	58.89	50.70	47.55
Critical Temperature (K)	2.61	2.62	2.29
Pauli Paramagnetic Limit H_P (kOe)	48.29	48.47	42.37
Spin-orbit Relaxation Time (10^{-13})	6.42	8.60	9.19

Table 4-2 Key parameters regarding critical fields and temperatures for the samples with different thicknesses.

52

REFERENCES

[1]   Kaveh Ahadi, Luca Galletti, Yuntian Li, Salva Salmani-Rezaie, Wangzhou Wu and Susanne Stemmer, *Sci. Adv.* 5, 4 (2019).

[2]   V. Celebonovic, J. Pesic, R. Gajic, BVasic and A. Matkovic, *J. Appl. Phys.* 125, 154301 (2019).

[3]   V. L. Ginzburg and L. D. Landau, *J. Exp. Theor. Phys.* (USSR) 20, 1064 (1950).

[4]   R. A. Klemn, A. Luther and M.R. Beasley *phys. Rev. B* 12, 3 (1975)

[5]   A. M. Clogston, *Phys. Rev. Lett.* 9, 6 (1962).

[6]   B. S. Chandrasekhat, *Appl. Phys. Lett.* 1, 1 (1962).

[7]   S.-T. Lo, S.-W. Lin, Y.-T. Wang, S.-D. Lin and C.-T. Liang, *Sci. Rep.* 4, 5438 (2014).

[8]   R. J. Elliott *Phys. Re.* 96 266 (1954).

Chapter 5   Conclusion
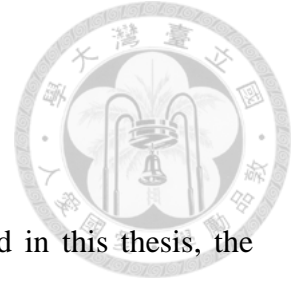
For the aluminum nanofilms grown by MBE which is studied in this thesis, the critical temperature and the critical magnetic field are both larger than those in bulk aluminum (1.2 K and 0.1 kOe).
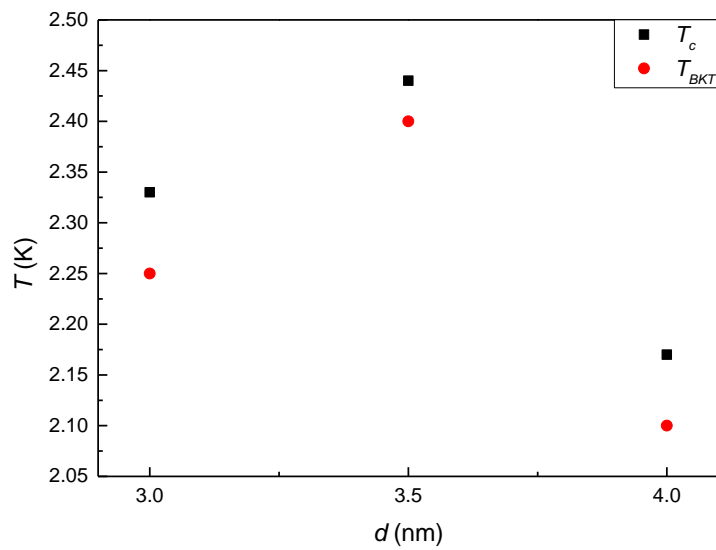

Figure 5.1 Critical temperature dependence on thickness $(T_c\text{-}d)$.

As shown in figure 5.1, although the increasing critical temperature can possible result from tensile strain, the critical temperature varies with thickness. It should be more studied how strain affect the critical temperature.
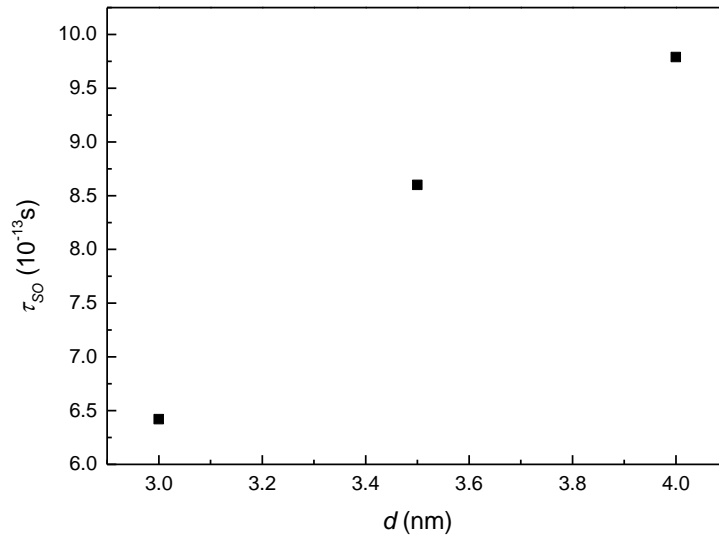
Figure 5.2 Spin-orbit relaxation time dependence on thickness.

As shown in figure 5.2, the spin-orbit relaxation time decrease with the decreasing thickness of Al nanofilm grown by MBE. The spin-orbit interaction can affect the upper critical magnetic field which is dominated by the Pauli limit.
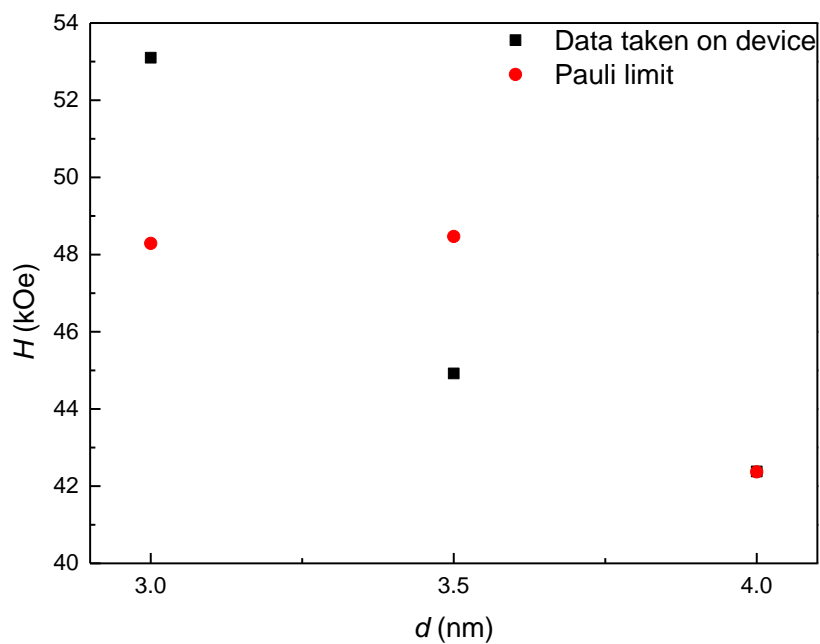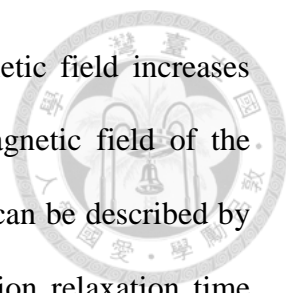

Figure 5.3 Parallel critical magnetic field dependence on thickness (d-H_c).

55

As shown in figures 5.3, the measured parallel critical magnetic field increases with decreasing film thickness. Moreover, the parallel critical magnetic field of the 3-nm-thick device slightly exceeds the Pauli paramagnetic limit. It can be described by spin-orbit interaction with EY mechanism. The spin-orbit interaction relaxation time decrease with decreasing thickness which may indicate the enhancement of Pauli paramagnetic limit by strong spin-orbit interaction.

WHH systematically theory studied the relation between the critical magnetic field and temperature with considering the orbital limit and spin paramagnetic limit simultaneously. However, the general solution is too complicated to deal with so it can be used to approximate with different simple case.

Chapter 6   Future Work
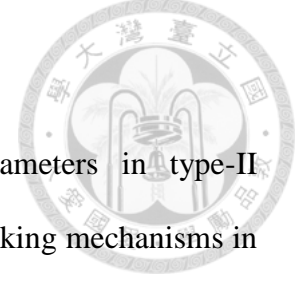
The upper critical field is one of the fundamental parameters in type-II superconductors, which provides important insights on the pair-breaking mechanisms in a magnetic field. Furthermore, other superconducting parameters, e.g., the coherence length and the anisotropic parameter, can be derived from the upper critical field.

The upper critical magnetic field is affected by the direction of applied magnetic field. In order to better characterize the anisotropy of the upper critical field, I propose to measure an Al nanofilm at different tilt angle, e.g. 30°, 45°, and 60°. The dependence of upper critical field can be well scaled by the single band anisotropic Ginzburg-Landau (G-L) theory [1]

$$\mu_0 H_{c2}^{GL}\left(\theta\right) = \frac{\mu_0 H_{c2}^{H_{\parallel c}}}{\sqrt{\cos^2\left(\theta\right) + \gamma^{-2}\sin^2\left(\theta\right)}},\tag{6.1}$$

where θ is the angle between the magnetic field and the c-axis. The anisotropic parameter γ is defined by $\gamma = \sqrt{\dfrac{m_{ab}}{m_c}} = \dfrac{H_{c2}^{H \perp c}}{H_{c2}^{H \parallel c}}$, where m_{ab} and m_c are the effective massed of electrons for the in-plane and out-of-plane motion, respectively.

Such a measurement may well shed light on how parallel magnetic field and/or perpendicular magnetic field can affect BKT superconductivity in our Al nanofilms. Moreover, it may well be related to the work on two-dimensional Ising superconductivity [2].

Different device structure can also greatly affect the critical magnetic field. It may be attributed to the ratio of magnetic length scale to device length scale [3]. I propose to study the critical magnetic field in Al nanofilms with different structures.

REFERENCES

[1] M. Tinkham, Introduction to Superconductivity 2nd edn (New York: McGraw-Hill), 1996.

[2] J. M. Lu, O. Zheliuk, I. Leermakers, N. F. Q. Yuan, U. Xeitler, K. T. Law, J. T. Ye *Science,* 350, 6266 (2015).

[3] Hyoungso Nam, Hua Chen, Philip W. Asams, Syu-You Guan, Tien Ming Chuang, Chia-Sheng Chang, Allan H. MacDonald and Chih-Kang Shih, *Nat. Commun.* 9, 5431 (2018).